The rupture extent of low frequency earthquakes near Parkfield, CA

Jessica C. Hawthorne (Department of Earth Sciences, University of Oxford, Oxford, UK)
Amanda M. Thomas (Department of Earth Sciences, University of Oregon, Oregon, USA)
Jean-Paul Ampuero (Université Côte d'Azur, IRD, CNRS, Observatoire de la Côte d'Azur, Géoazur, France)

Manuscript submitted to *Geophysical Journal International*

Abstract

The low frequency earthquakes (LFEs) that constitute tectonic tremor are often inferred to be slow: to have durations of 0.2 to 0.5 s, a factor of 10 to 100 longer than those of typical M_W 1-2 earthquakes. Here we examine LFEs near Parkfield, CA in order to assess several proposed explanations for LFEs' long durations. We determine LFE rupture areas and location distributions using a new approach, similar to directivity analysis, where we examine how signals coming from various locations within LFEs' finite rupture extents create differences in the apparent source time functions recorded at various stations. We use synthetic ruptures to determine how much the LFE signals recorded at each station would be modified by spatial variations of the source-station travel time within the rupture area given various possible rupture diameters, and then compare those synthetics with the data. Our synthetics show that the methodology can identify inter-station variations created by heterogeneous slip distributions or complex rupture edges, and thus lets us estimate LFE rupture extents for unilateral or bilateral ruptures. To obtain robust estimates of the sources' similarity across stations, we stack signals from thousands of LFEs, using an empirical Green's function approach to isolate the LFEs' apparent source time functions from the path effects. Our analysis of LFEs in Parkfield implies that LFEs' apparent source time functions are similar across stations at frequencies up to 8 to 16 Hz, depending on the family.

The inter-station coherence observed at these relatively high frequencies, or short wavelengths (down to 0.2 to 0.5 km), suggest that LFEs in each of the 7 families examined occur on asperities. They are clustered in patches with sub-1-km diameters. The individual LFEs' rupture diameters are estimated to be smaller than 1.1 km for all families, and smaller than 0.5 km and 1 km for the two shallowest families, which were previously found to have 0.2-s durations. Coupling the diameters with the durations suggests that it is possible to model these M_W 1-2 LFEs with earthquake-like rupture speeds: around 70% of the shear wave speed. However, that rupture speed matches the data only at the edge of our uncertainty estimates for the family with highest coherence. The data for that family are better matched if LFEs have rupture velocities smaller than 40% of the shear wave speed, or if LFEs have different rupture dynamics. They could have long rise times, contain composite sub-ruptures, or have slip distributions that persist from event to event.

1 Introduction

Tectonic tremor is a long-duration seismic signal, best observed at frequencies between 1 and 10 Hz (e.g., *Obara*, 2002; *Rogers and Dragert*, 2003; *Payero et al.*, 2008; *Peterson and Christensen*, 2009; *Rubinstein et al.*, 2009; *Fry et al.*, 2011). It is thought to consist of numerous small low frequency earthquakes, or LFEs (*Shelly et al.*, 2006, 2007; *Wech and Creager*, 2007; *Brown et al.*, 2009). LFEs are often inferred to have magnitudes between M_W 1 and 2.5 but to have corner frequencies of a few Hz, a factor of 10 to 100 times smaller than corner frequencies observed for "normal" M_W 1-2.5 earthquakes (*Fletcher and McGarr*, 2011; *Zhang et al.*, 2011; *Bostock et al.*, 2017). LFEs are found to have durations around 0.2 seconds in Parkfield (*Thomas et al.*, 2016) and around 0.5 s in Cascadia (*Bostock et al.*, 2015), which are a factor of 10 to 100 longer than "normal" M_W 1-2.5 earthquakes.

1.1 Potential Causes of LFEs' Long Durations

The durations of typical earthquakes are determined by their spatial extent: by how long it takes the rupture to progress across the earthquake area. Models and observations suggest that earthquake ruptures usually progress at speeds of 2 to 3 km/s, or 60 to 95% of the shear wave speed V_s (*Kanamori and Brodsky*, 2004; *McGuire*, 2004; *Madariaga*, 2007; *Seekins and Boatwright*, 2010; *Taira et al.*, 2015; *Folesky et al.*, 2016; *Ye et al.*, 2016; *Melgar and Hayes*, 2017; *Chounet et al.*, 2018). Earthquakes' durations can thus be roughly estimated by dividing their rupture lengths by the shear wave speed. If LFEs, like normal earthquakes, rupture at speeds close to the shear wave speed, their long durations could indicate that LFEs have unusually large lengths given their moment: perhaps 0.7 to 1.5 km. In this scenario, LFEs would have lower stress drops than normal earthquakes—0.1 to 10 kPa, but they could otherwise be governed by the same physical processes. LFEs could be driven by unstable frictional sliding, and their slip speeds could be limited by the energy that they dissipate via seismic waves (e.g., *Rice*, 1980; *Kanamori and Brodsky*, 2004).

However, it is also possible that seismic wave generation has minimal impact on LFE dynamics, and that LFEs are governed by different fault zone processes. LFEs' slip rates may be limited by a spatial constraint or by a speed-limiting frictional rheology (e.g., *Liu and Rice*, 2005, 2007; *Shibazaki and Shimamoto*, 2007; *Rubin*, 2008; *Segall et al.*, 2010; *Skarbek et al.*, 2012; *Fagereng et al.*, 2014; *Yabe and Ide*, 2017). For instance, LFEs might occur on faults with a velocity-strengthening rheology, which inhibits increases in slip rate. The brief slip rate increases seen in LFEs could result from imposed local stress concentrations, perhaps created by the creep fronts of large slow slip events (e.g., *Perfettini and Ampuero*, 2008; *Rubin*, 2009). Alternatively, LFEs could occur on faults with a more complex rheology, which encourages initial increases in slip rate but inhibits slip rates higher than some cutoff speed. Such rheologies are commonly proposed for slow slip events and may be created by shear-induced dilatancy or by a minimum asperity size (e.g., *Shibazaki and Iio*, 2003; *Shibazaki and Shimamoto*, 2007; *Liu et al.*, 2010; *Segall et al.*, 2010; *Hawthorne and Rubin*, 2013; *Poulet et al.*, 2014). The possibility that LFEs are small versions of slow slip events is intriguing because slip rates vary widely from slow slip to tremor (*Ide et al.*, 2007, 2008; *Aguiar et al.*, 2009; *Gao et al.*, 2012; *Ide and Yabe*, 2014; *Hawthorne and Bartlow*, 2018). Several of the processes proposed to govern slow slip would have difficulty producing such a wide range of slip rates (e.g., *Liu and Rice*, 2005, 2007; *Shibazaki and Shimamoto*, 2007; *Hawthorne and Rubin*, 2013; *Fagereng et al.*, 2014; *Veveakis et al.*, 2014). If LFE slip rates are

limited primarily by frictional resistance to shear and not by seismic wave radiation, LFEs need not rupture across the fault at speeds close to the shear wave speed. They could rupture more slowly and have diameters far smaller than 1 km despite their 0.2-s durations.

LFEs could also have small rupture diameters if their 0.2-s durations and low corner frequencies are actually apparent values, not true ones. LFEs could be "normal" M_W 1-2.5 earthquakes, with 0.01-s durations and 10-m rupture diameters. They may appear to be dominated by low-frequency signals only because their high-frequency signals are attenuated when they pass through a highly damaged fault zone or through a region of high pore fluid pressure (*Gomberg et al.*, 2012; *Bostock et al.*, 2017). Regions of high pore pressure or increased attenuation are frequently identified near the slow slip region (*Audet et al.*, 2009; *Song et al.*, 2009; *van Avendonk et al.*, 2010; *Kato et al.*, 2010; *Fagereng and Diener*, 2011; *Kitajima and Saffer*, 2012; *Nowack and Bostock*, 2013; *Yabe et al.*, 2014; *Saffer and Wallace*, 2015; *Audet and Schaeffer*, 2018), though we note that any regions with attenuation strong enough to produce tremor's frequency content might have to be localized into patches. Earthquakes do occur below the tremor-generating region, and some of them show higher-frequency signals than tremor (*Seno and Yamasaki*, 2003; *Shelly et al.*, 2006; *Bell et al.*, 2010; *Kato et al.*, 2010; *Gomberg et al.*, 2012; *Bostock et al.*, 2017).

1.2 Potential Role of Tremor Asperities

Tremor is often patchily distributed along the plate interface; it is densely concentrated in some regions but appears absent in others (e.g., *Payero et al.*, 2008; *Maeda and Obara*, 2009; *Walter et al.*, 2011; *Ghosh et al.*, 2012; *Armbruster et al.*, 2014). Some observations and models suggest that tremor occurs only on a set of tremor-generating asperities (e.g., *Ariyoshi et al.*, 2009; *Ando et al.*, 2010; *Shelly*, 2010b; *Nakata et al.*, 2011; *Ando et al.*, 2012; *Sweet et al.*, 2014; *Veedu and Barbot*, 2016; *Chestler and Creager*, 2017a,b; *Luo and Ampuero*, 2017). Such asperities may also be suggested by the success of template matching approaches to tremor identification, in which LFEs are detected and grouped into families according to waveform similarity. Each LFE family could reflect an individual tremor asperity (*Shelly et al.*, 2007; *Brown et al.*, 2008; *Bostock et al.*, 2012; *Frank et al.*, 2013; *Kato*, 2017; *Shelly*, 2017). However, the family grouping could also result from more gradual variations in the path effects. LFEs located more than 1 or a few km away from each other may be grouped into distinct families simply because the path effects vary significantly on several-km length scales, so that well-separated LFEs give rise to distinct seismograms.

A few studies have provided further indications that LFE families reflect tremor clusters. *Sweet et al.* (2014) relocated LFEs within an isolated family in Cascadia and found that they clustered within a 1-km-wide patch. *Chestler and Creager* (2017b) relocated LFEs within around 20 families in Cascadia and found that LFEs cluster within 1 to 2-km-wide patches that are often separated by > 5-km-wide areas with few to no LFEs. Tremor-generating asperities are also suggested by the highly repetitive recurrence intervals of one isolated LFE family near Parkfield, CA, which suggest that the LFEs could be repeating similar ruptures of a particular asperity (*Shelly*, 2010b; *Veedu and Barbot*, 2016). Repetitive LFE rupture is also suggested by LFE moments and durations that vary little from event to event, creating exponential amplitude distributions (*Watanabe et al.*, 2007; *Shelly and Hardebeck*, 2010; *Chamberlain et al.*, 2014; *Sweet et al.*, 2014; *Bostock et al.*, 2015; *Chestler and Creager*, 2017a), though it is also possible that each LFE ruptures only a portion of a tremor-generating asperity. The total slip on an LFE patch could result from a range of ruptures of different types, as well as some aseismic slip (*Chestler and Creager*, 2017a).

1.3 Analysis to Be Presented

In this study, we further assess whether small asperities control tremor generation and whether LFEs are governed by earthquake-like or slow slip rheologies by determining the rupture extents of LFEs in seven families near Parkfield, CA. We will place upper bounds on the spatial distribution of LFEs in each family and on the average LFE rupture area. In order to obtain these bounds, we will introduce a new coherence-based approach, which can be thought of as a version of directivity analysis that we have modified so that we can combine data from thousands of LFEs which may rupture unilaterally or bilaterally (e.g. *Mueller*, 1985; *Mori and Frankel*, 1990; *Got and Fréchet*, 1993; *Velasco et al.*, 1994; *Lengliné and Got*, 2011; *Wang and Rubin*, 2011; *Kane et al.*, 2013). We examine how signals coming from various locations within LFEs' finite rupture areas can produce complex apparent source time functions (ASTFs) that vary from station to station. We quantify the ASTF variation as a function of frequency, or seismic wavelength, in order to determine the LFE rupture area.

We qualitatively explain how the ASTFs' frequency-dependent variability should reflect LFEs' rupture extents in section 2. In section 3, we present our approach in more detail. We describe how we can isolate the ASTFs from observed seismograms using an empirical Green's function approach and then how we can quantify the ASTFs' coherence among LFEs and among stations. In sections 4 and 5, we analyze ASTF coherence for individual LFEs near Parkfield and then average over thousands of LFEs to obtain well-resolved estimates of inter-station coherence as a function of frequency. For comparison, we also compute ASTF coherence for a suite of synthetic LFEs with a range of diameters and rupture velocities (section 6). Finally, in sections 7 and 8, we compare the data with the synthetics to determine which rupture areas are plausible and which types of LFEs could match the observations.

2 Premise: Mapping Inter-Station Similarity to Rupture Area

In order to estimate LFE areas, we note that seismic waves generated at a range of locations throughout the source region require different amounts of time to travel to the various stations. For instance, in the rupture illustrated in Figure 1d, seismic waves generated by the high-slip asperity marked in red arrive earliest at the NW station (left) because the asperity is in the northwestern half of the rupture. But waves generated at the blue asperity, located farther SE, arrive first at the SE station. The time-shifted signals give rise to apparent source time functions (ASTFs) that differ among the recording stations, as seen in Figure 1a-c.

If we assume that Earth structure is relatively uniform within the source region, we may account for the travel time variations by modeling the observed seismograms d_k in terms of station-specific apparent source time functions s_k. At each station k,

$$\hat{d}_k(\omega) = \hat{s}_k(\omega)\hat{g}_k(\omega). \tag{1}$$

Here g_k is an average Green's function for the source area, and $\hat{d}_k$, $\hat{s}_k$, and $\hat{g}_k$ are the Fourier coefficients of d_k, s_k, and g_k, respectively.

If we define $g_k(t)$ as the Green's function for a signal generated at a reference location x_0, $\Delta t_k(x)$ as the source-station travel time for a signal generated at location x, and $\dot{\delta}(x,t)$ as the slip rate as a function of location x and time t, then the ASTF can be obtained by integrating over all

points x within the rupture area:

$$s_k(t) = \int_{\text{rupture area}} \dot{\delta}(x, t - \Delta t_k(x) + \Delta t_k(x_0))dA. \quad (2)$$

The coloring in Figure 1 shows how three slip asperities shown contribute to ASTFs that differ among stations located to the northwest, southeast, and above the earthquake. Note that the asperities create differences at all three stations even though the earthquake ruptures radially out from the center point.

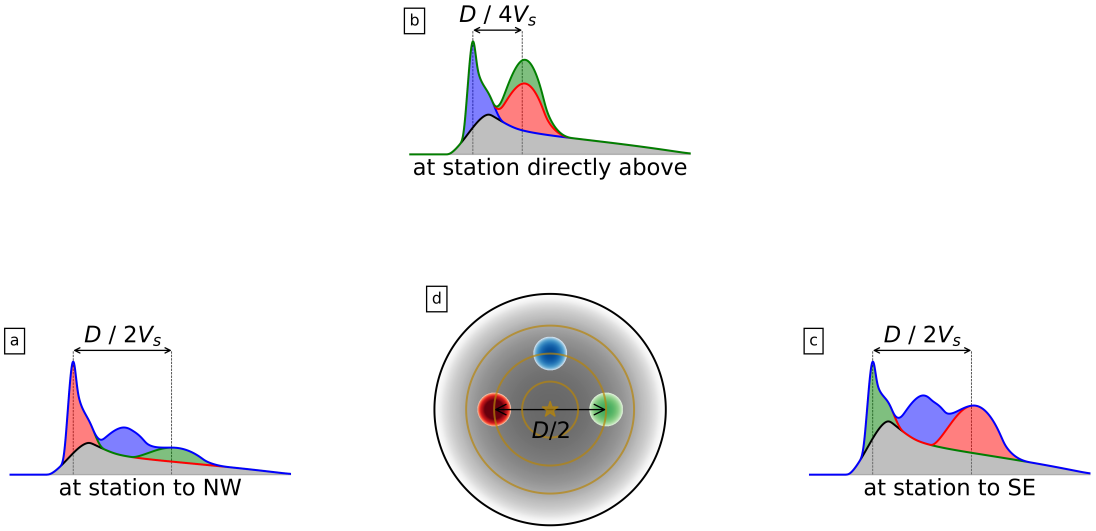

Figure 1: (a-c) ASTFs observed at 3 stations due to rupture of the slip distribution illustrated in panel (d). Rupture progresses outward from the center and moves through 3 high-slip asperities of varying magnitude, illustrated with colored circles. The asperities generate seismic waves which require different amounts of time to travel to the stations, giving rise to the various colored peaks in the ASTFs. Note that the timing of the asperity-created peaks varies among the stations by up to $D/2V_s$: half the rupture diameter divided by the shear wave speed.

There is, however, a limit to the ASTF differences. The spatially variable source-station travel time may shift peaks in this earthquake's source time function by only a limited amount: up to D/V_s, the rupture diameter D divided by the seismic wavespeed V_s. Thus we can see differences in the ASTFs only if we examine their short-period signal. If we examine ASTFs at periods much longer than D/V_s, the travel time shifts will be a small fraction of the period, and the ASTFs will be roughly the same at all stations. Synthetic rupture models described in section 6 show that ASTFs are similar among stations at periods longer than 0.45 to $1.4D/V_s$. Here the range of limiting periods results from the earthquakes' other rupture parameters, but we note that periods at which ASTFs are similar depend primarily on the diameter divided by seismic wave speed V_s, not on the diameter divided by the LFEs' rupture speed V_r. We will thus be able to use the ASTFs' frequency-dependent similarity to estimate LFE rupture extents without making restrictive assumptions about LFE rupture dynamics.

3 Quantifying Coherence Across Events and Stations

3.1 Removing the Path Effect

In order to examine ASTFs, we must first isolate them from the observed seismograms. To do so, we use an empirical Green's function approach similar to that of *Hawthorne and Ampuero* (2017) and compare each LFE's seismograms with a template event created via stacking (a variant on, e.g., *Mueller*, 1985; *Mori and Frankel*, 1990; *Velasco et al.*, 1994; *Hough*, 1997; *Prieto et al.*, 2004; *Baltay et al.*, 2010; *Kwiatek et al.*, 2011; *Uchide et al.*, 2014). The individual and template LFEs' seismograms d_{jk} and d_{tk} can be approximated as convolutions of ASTFs s_{jk} or s_{tk} and Green's functions g_k, so that

$$\hat{d}_{jk}(\omega) = \hat{s}_{jk}(\omega)\hat{g}_k(\omega). \tag{3}$$

To isolate the ASTFs from the Green's functions, we compute the normalized cross-spectrum $\hat{x}_{jk}$ of the individual and template recordings:

$$\hat{x}_{jk} = \frac{\hat{d}_{jk}\hat{d}^*_{tk}}{|\hat{d}^*_{tk}|^2} = \frac{\hat{s}_{jk}\hat{s}^*_{tk}|\hat{g}_k|^2}{|\hat{s}_{tk}|^2|\hat{g}_k|^2} = \frac{\hat{s}_{jk}\hat{s}^*_{tk}}{|\hat{s}_{tk}|^2}, \tag{4}$$

where we have omitted the frequency indexing for readability. In the second equality, we have assumed that the template LFE has the same Green's functions as the individual event, so that the path effects cancel out, and we are left with a function that depends on the relative amplitudes and phases of the individual and template ASTFs. Note that we always normalize by the template amplitude, as this will allow us to stack ASTFs from thousands of LFEs. We will use the cross-spectra $\hat{x}_{jk}$ to examine how ASTFs' amplitudes and phases vary among LFEs j and stations k.

3.2 ASTF Energy: Direct and Inter-Station Coherence

As a first step, we ignore inter-station variations, and simply examine how much LFE source time functions vary from event to event. We assess the similarity between the individual and template ASTFs by computing the directly coherent power for each LFE j

$$P_d = \frac{1}{N}\sum_{k=1}^{N} a_{jk}^2 \left[\mathrm{Re}\left(\hat{x}_{jk}\right)\right]^2 \mathrm{sgn}\left[\mathrm{Re}\left(\hat{x}_{jk}\right)\right] \tag{5}$$

$$= \frac{1}{N}\sum_{k=1}^{N} a_{jk}^2 \left[\mathrm{Re}\,\frac{\hat{s}_{jk}\hat{s}^*_{tk}}{|\hat{s}_{tk}|^2}\right]^2 \mathrm{sgn}\left[\mathrm{Re}\left(\hat{s}_{jk}\hat{s}^*_{tk}\right)\right]. \tag{6}$$

Here the coefficients a_{jk} represent an optional weighting of the observed signals. The equality in equation (6) assumes that the individual LFE and the template have the same path effects. If the individual and template LFEs also have similar and well-aligned ASTFs $\hat{s}_{jk}$ and $\hat{s}_{tk}$, the value $\hat{s}_{jk}\hat{s}^*_{tk}$ in equation (6) will be real and positive. The directly coherent power P_d is thus also positive when the individual and templates ASTFs are the same. Its amplitude is determined by the relative power of the individual and template ASTFs.

The relative ASTF power also determines the amplitude of the inter-station coherent power P_c. With this power calculation, we seek to ignore ASTF variations across events, and instead assess

the ASTFs' similarity across stations. So we compute

$$P_c = \frac{2}{N(N-1)} \sum_{k=1}^{N} \sum_{l=k+1}^{N} a_{jk} a_{jl} \operatorname{Re}\left(\hat{x}_{jk} \hat{x}_{jl}^*\right) \tag{7}$$

$$= \frac{2}{N(N-1)} \sum_{k=1}^{N} \sum_{l=k+1}^{N} a_{jk} a_{jl} \operatorname{Re} \frac{\left(\hat{s}_{jk} \hat{s}_{jl}^*\right) \left(\hat{s}_{tk}^* \hat{s}_{tl}\right)}{|\hat{s}_{tk}|^2 |\hat{s}_{tl}|^2}, \tag{8}$$

where the second equality again assumes common path effects. As noted in section 2, the ASTFs are expected to be the same for all stations if the period being considered with these Fourier coefficients is long compared with D/V_s, the intra-source seismic wave travel time. If the ASTFs are the same across stations at the period of interest, we will have $\hat{s}_{jk} = \hat{s}_{jl}$ and $\hat{s}_{tk} = \hat{s}_{tl}$, so that $\hat{s}_{jk}\hat{s}_{jl}^*$, $\hat{s}_{tk}^*\hat{s}_{tl}$, and finally P_c are all real and positive.

P_d and P_c thus give us estimates of the direct or inter-station coherent power of an LFE, as normalized by the template power. However, we can obtain a more interpretable normalization if we also estimate the full template-normalized LFE power, including any incoherent components:

$$P_l = \frac{1}{N} \sum_{k=1}^{N} a_{jk}^2 |\hat{x}_{jk}|^2 \tag{9}$$

$$= \frac{1}{N} \sum_{k=1}^{N} a_{jk}^2 \frac{|\hat{s}_{jk}|^2}{|\hat{s}_{tk}|^2}. \tag{10}$$

We will use the LFE power P_l to normalize P_d and P_c and compute the fraction of the power that is coherent across events and stations.

4 Calculating Powers of Parkfield LFEs

When we extract the coherent and incoherent powers of LFEs near Parkfield, we will also have to estimate and remove the noise, and we will have to average over thousands of LFEs to obtain well-resolved powers. To begin, we describe the LFE catalog and seismic data (section 4.1) and create templates for seven LFE families (section 4.2). Then we demonstrate our approach by estimating template-normalized powers for an individual LFE (section 4.3). Finally, we average the powers over the LFEs in each family (section 5).

4.1 Data and LFE Families

The LFEs considered here occurred between 2006 and 2015 at depths of 16 to 23 km near Parkfield, CA (see Figure 2). They were identified via cross-correlation by *Shelly* (2017) as part of his 15-year tremor catalog and are grouped into seven families numbered 37140, 37102, 70316, 27270, 45688, 77401, and 9707, with 2500 to 8300 LFEs in each family (see also *Shelly et al.* (2009); *Shelly and Hardebeck* (2010)). LFEs in families 37140 and 37102 were examined by *Thomas et al.* (2016) and found to have best-fitting source durations of 0.19 and 0.22 s, respectively. We use LFE seismograms from 17 borehole seismic stations in the Berkeley HRSN (High Resolution

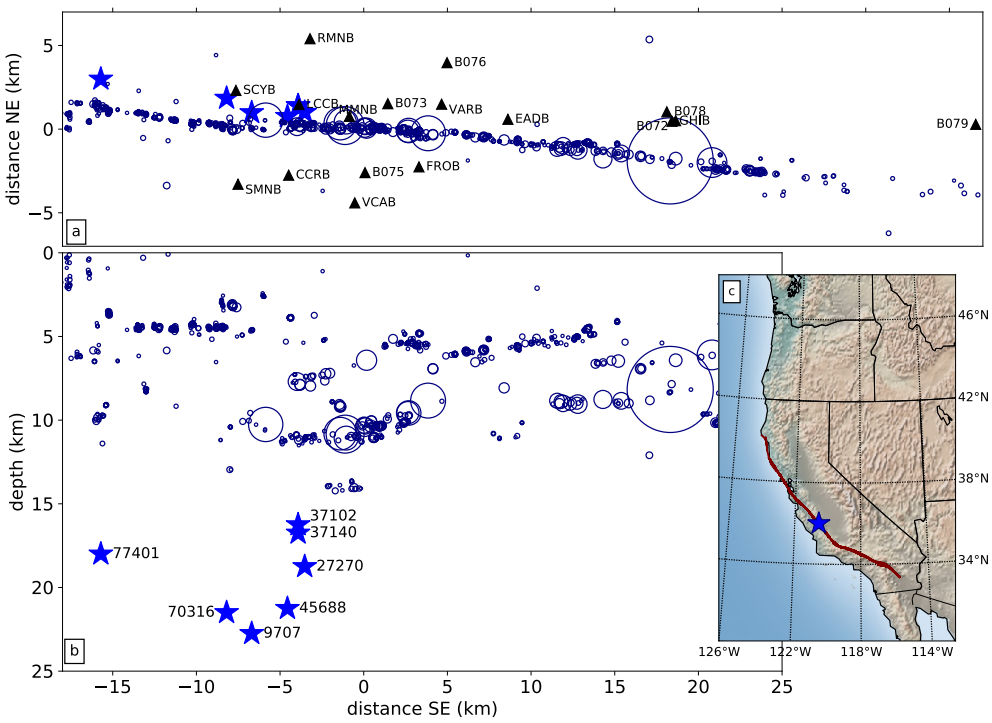

Figure 2: (a) Map view and (b) depth section of the LFE families (blue stars), local $M > 2.5$ earthquakes (circles), and the HRSN and PBO seismic stations used (triangles). Earthquake sizes are scaled to the radii expected for 3-MPa stress drops, and locations are taken from the NCEDC catalog and the relocations of *Waldhauser* (2009).

Seismic Network) and in the PBO (Plate Boundary Observatory) network. Since this analysis relies on high-quality recordings of small LFEs, we correct the data for some errors identified by *Shelly* (2017). We have also gone through the data from each station and channel and discarded weeks- to years-long intervals where the LFE amplitudes are much more scattered than usual, as these intervals likely have larger-than-average noise.

4.2 Stacked LFE Templates

For each LFE family, we create a low-noise template by averaging the LFE records for each channel. We bandpass filter the LFE seismograms from 2 to 30 Hz, normalize them by their maximum values, and then average, weighting each record by the station-averaged cross-correlation coefficient obtained by *Shelly* (2017). Then we rescale these normalized stacks so that their amplitudes match the amplitudes of individual records, as described in section S2. We iterate the stack a few times to slightly improve the signal to noise ratio, each time discarding records with very small or unusual amplitudes (for details see section S2).

We estimate the signal to noise ratio of the stacks using a 3-second window starting just before the S arrival. We keep only the stacks which have average amplitude spectra at least 3 times larger than the noise in the 2 to 10 Hz band. The procedure leaves us with 16 to 29 well-resolved template seismograms for each LFE family, observed on the two horizontal components of 9 to 16 stations. Some are shown in Figure 3a, as well as in Figures S1 to S7.

4.3 Coherent and Total Powers for One LFE

We will use the obtained templates to remove the Green's functions from individual LFE records, so that we can probe the LFEs' ASTFs. To prepare, we realign each LFE's origin time to better match the template, as poor alignment could reduce the direct coherence P_d. We bandpass filter to 2 to 5 Hz, cross-correlate to obtain a preferred shift at each station, and then shift the seismograms of all stations by the median shift.

Next, we remove the path effects for the power calculations. We extract 3-second-long segments of the template seismograms, starting just before the S arrival, and cross-correlate the segments with the individual LFE records. The individual LFE records are truncated 0.2 seconds before the S arrival to reduce contamination by the P arrival, but they are not truncated after the S wave. We average the cross-correlations over the available channels at each station.

Cross-correlations obtained for one LFE are illustrated in Figure 3b. The cross-correlations are often roughly but not entirely symmetric, suggesting that the individual and template LFEs have slightly different source time functions. The asymmetry is also apparent in the non-zero phases of the cross-correlations' Fourier coefficients, which are equal to the phases of the normalized cross-spectra $\hat{x}_{jk}$ (equation (4), Figure 3c). To estimate the $\hat{x}_{jk}$, we first extract a 6-second portion of the cross-correlations, multiply by a Slepian taper concentrated at frequencies lower than 0.4 Hz, and compute the Fourier transform (*Thomson*, 1982). Then we normalize; we divide by the Fourier transform of the template seismograms' autocorrelation, computed via the same procedure.

We use the cross-spectra to compute the power that is directly coherent (P_d, equation (5)) and coherent among stations (P_c, equation (7)) and plot them in yellow and red in Figure 3d. The total power P_t in the template-normalized cross-correlation is also computed, following equation (9), and is plotted in green. However, a significant fraction of this total power comes from noise, not from the LFE signal. To estimate the noise contribution, we cross-correlate the template seismograms with data from noise intervals starting 8 seconds before the S arrivals. We compute the power (P_n) in those noise correlations, again following equation (9), and plot it in gray in Figure 3d. Finally, we subtract the noise power P_n from the total power P_t to determine the power contributed by the LFE (P_l, blue in Figure 3d).

In all the power calculations, we use weightings a_{jk} equal to one over the standard deviation of the 2 to 30-Hz filtered waveform, as computed in the four seconds ending 0.5 s before the LFE S arrival. This weighting allows us to downweight records with large noise, but it does not bias our results because all of the power in P_t, P_c, and P_d comes from after 0.2 s before the S arrival and because almost all of the subtracted noise power P_n comes from more than 5 seconds before the S arrival.

In an ideal scenario, we would now interpret the estimated powers, and compare the coherent powers P_d and P_c with the LFE power P_l. However, for this and other individual LFEs, the powers are too poorly resolved to allow direct interpretation. In Figure 3d, the ratios P_d/P_l and P_c/P_l vary by tens of percent among the frequencies but show no systematic trend, and there is further variation if we use different subsets of the stations. So in the next section, we will average the powers over several thousand LFEs to obtain well-resolved and stable coherent power fractions.

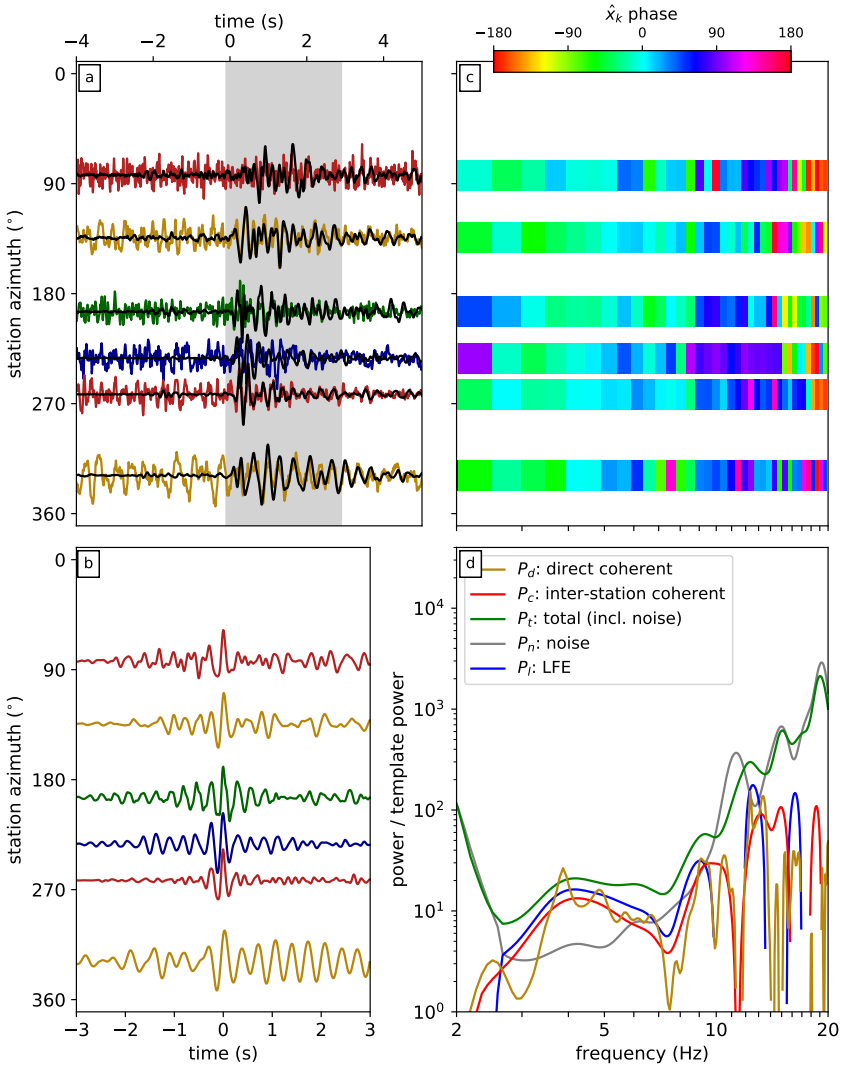

Figure 3: (a) Some of the template seismograms (black) for family 37102 along with seismograms observed for one LFE (color). Traces are organized according to the station's azimuth relative to the LFE and are scaled to their maximum value. The gray shading indicates the portion of the template that is correlated with the individual observations. (b) Cross-correlations of the observed seismograms with the template. (c) Phase of the cross-spectra: of the Fourier coefficients of the cross-correlations in panel b. (d) Yellow, red, and green curves: P_d, P_c, and P_t—the coherent and total template-normalized powers from the LFE interval. Gray: P_n—the noise power, computed in an interval without the LFE. Blue: $P_l = P_t - P_n$—the power likely contributed by the LFE. Note that with just this one LFE, it is not practical to interpret the relative values of the coherent and total powers.

5 Results: Event-Averaged Coherent and Incoherent Powers

To estimate P_c, P_d, P_t, and P_n for a given family of LFEs, we compute the powers for individual events and then average. However, some LFE records have exceptionally large noise, so we check the signals' amplitudes before the calculation and discard records when the S arrival or the preceding noise interval has standard deviation that differs by more than a factor of 10 from that channel's median. This record selection, coupled with data availability, leaves us with 860 to 4220 LFEs per family which have template-normalized powers computed from at least 5 stations.

Figure 4a shows the summed coherent and total powers obtained from 2000 LFEs in family 37140, one of the two families with duration estimates from *Thomas et al.* (2016). The shading indicates 95% uncertainty ranges on the powers, obtained by bootstrapping the LFEs included in the summation. All of the template-normalized powers increase with frequency, suggesting that the high-frequency template power is damped relative to a typical LFE. The stacks' high-frequency signal may be averaged out by stacking if LFEs are more different at higher frequencies or if the LFE timing is not accurate enough to allow coherent stacks at higher frequencies. The stacking effectively creates a template LFE which has slightly broader and simpler ASTFs (*Royer and Bostock*, 2014). Note that this ASTF modification may reduce the direct coherence between the template and the individual LFEs P_d, but it should not affect the inter-station coherence P_c, as P_c is independent of inter-event ASTF differences.

We compute the coherent power fractions P_d/P_l and P_c/P_l for all 7 families and plot the results in Figure 4b-h. For family 37140 (panel b), the direct coherence P_d/P_l is larger than 0.8 at frequencies of 2 to 4 Hz, suggesting that most 0.2-second-long LFE source time functions are similar when viewed at these frequencies. We should note, however, that P_d/P_l may be slightly higher than its true value in this range because we allowed for an LFE origin time shift using data in the 2 to 5-Hz range. P_d/P_l decreases at higher frequencies, falling below 0.6 at a frequency of 5 Hz. The decrease in direct coherence could imply (1) that the LFE source time functions are more different at higher frequencies, (2) that the LFEs are too poorly aligned to show direct coherence at high frequencies, or (3) that the stacking has modified the source time functions being compared. We have tried improving the alignment by using higher-frequency signals in the alignment cross-correlation, outside the 2 to 5-Hz range. We find that the high-frequency signals does result in large P_d/P_l out to higher frequencies, but we choose not to use it here because some of the increase in P_d/P_l could come from the alignment of high-frequency noise.

Family 37140's inter-station coherent power P_c/P_l is insensitive to the alignment, and it remains coherent over a wider frequency range. P_c/P_l is above 0.8 at frequencies up to 12 or 15 Hz and falls below 0.6 only at 16.5 Hz. The persistence of high P_c/P_l out to frequencies $>$15 Hz suggests that the ASTFs vary little among stations at $>$0.07-second periods. We will use synthetic rupture calculations to interpret this high-frequency coherence in terms of LFE rupture area in section 7.

The other six LFE families show similar or slightly lower coherence, as seen in Figure 4c-h and in Figures S8 - S14. Family 37102, the other family with an estimated duration (*Thomas et al.*, 2016), displays gradually decaying P_d/P_l and P_c/P_l (Figures 4b and S9). Its P_d/P_l falls below 0.6 at 4 Hz, and its P_c/P_l stays above or hovers near 0.6 until 9 Hz. For the remaining families, the direct coherence P_d/P_l remains above 0.6 out to 4 to 5 Hz. The inter-station coherence P_c/P_l remains above 0.6 out to 8 to 13 Hz: to 8, 9, 11, 12, and 13 Hz.

These high-coherence frequency limits are likely lower bounds on the true high-coherence fre-

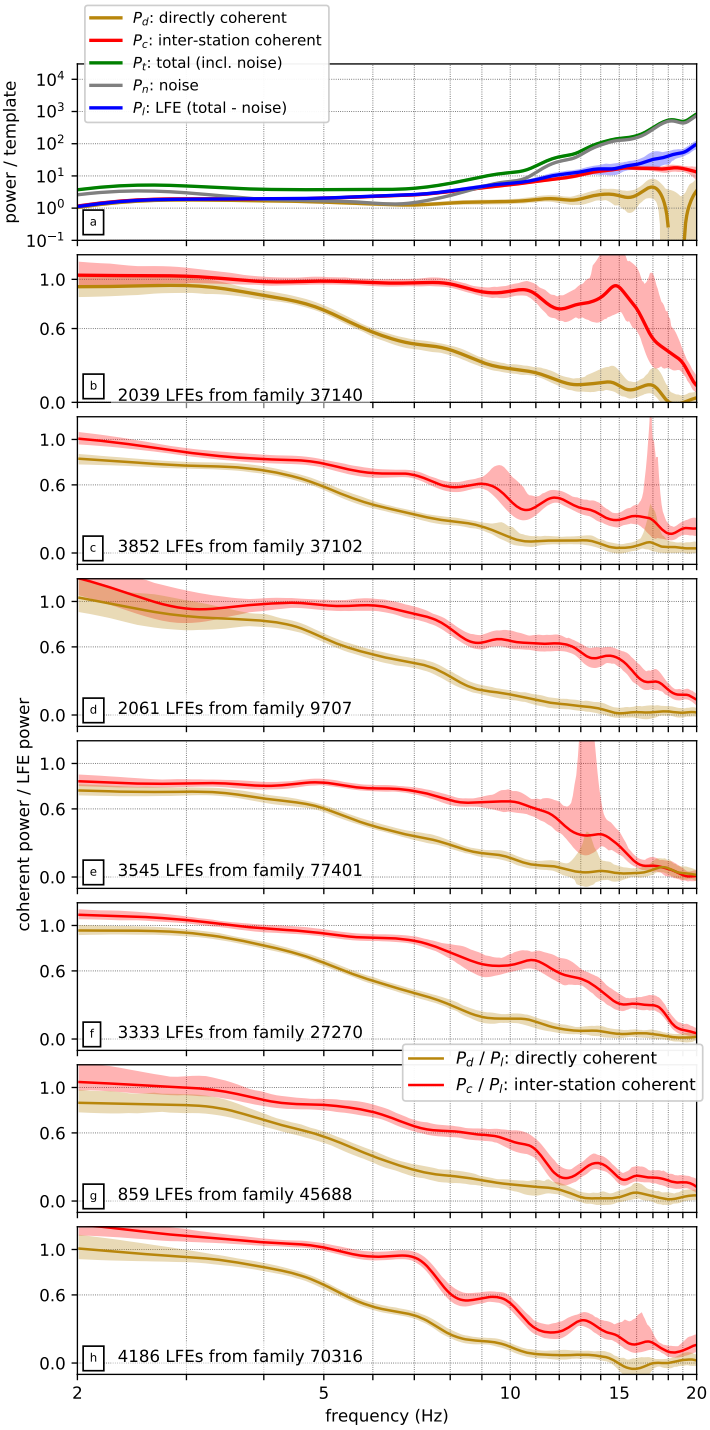

Figure 4: (a) Coherent and incoherent powers, as in Figure 3d, but averaged over 2000 LFEs from family 37140. Color indicates the power of interest. In all panels, the line indicates the value obtained with all allowable LFEs, and the shaded region delimits 95% confidence intervals obtained by bootstrapping the included events. (b-h) Ratios of the direct and inter-station coherence: P_c/P_l (yellow) and P_d/P_l (red). Each panel is computed for a different LFE family, as indicated by the text in the bottom left.

quencies. Our coherence estimates could be affected by several factors, including LFE clustering, data selection, LFE origin time alignment, and template accuracy. We describe the uncertainties in Appendix A1 and note that only the LFE origin time alignment is likely to give artificially high coherence, and it affects only P_d/P_l, not P_c/P_l. The remaining factors would result in our underestimating the true P_d/P_l and P_c/P_l. In section 7, we will therefore interpret our coherence estimates as lower limits when we consider their implications for LFE rupture areas and location distributions.

6 Frequencies With Coherent Power: Synthetics

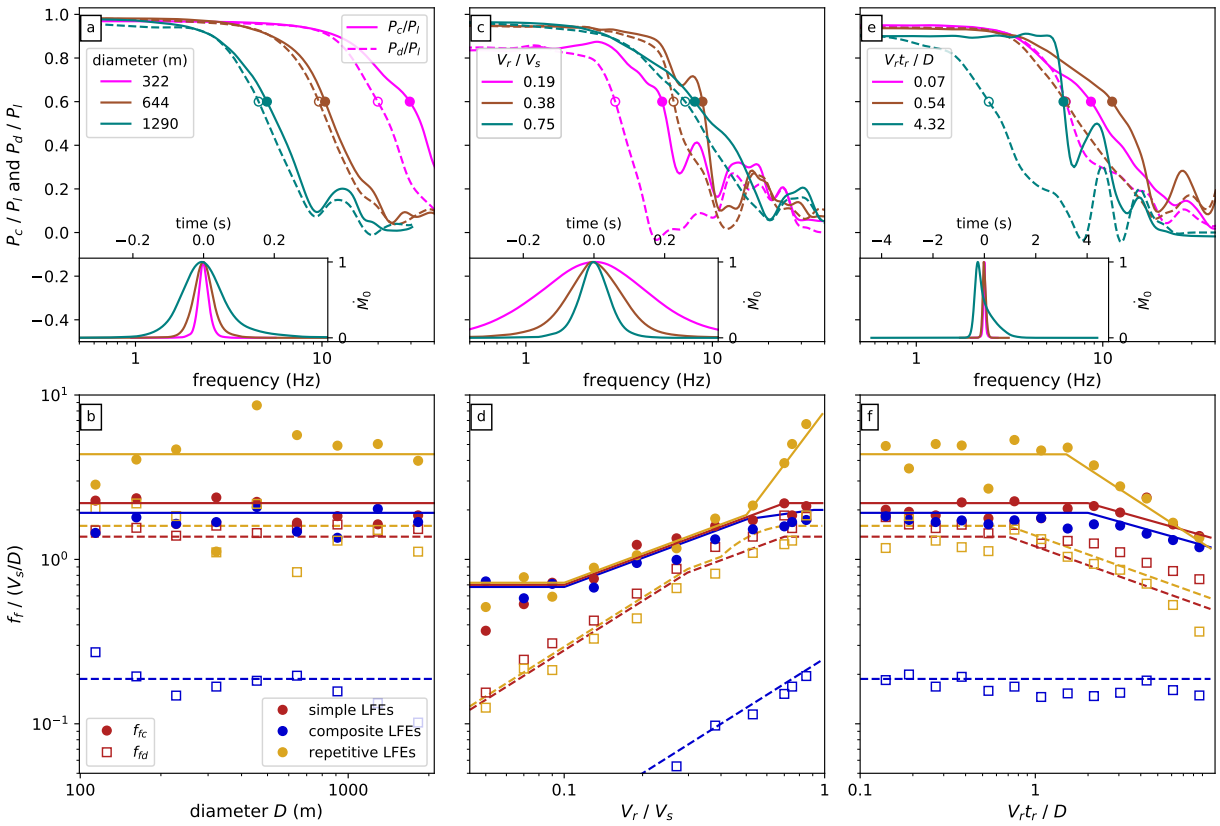

Figure 5: (a, c, e) Coherent power fractions P_c/P_l (solid lines) and P_d/P_l (dashed lines) as a function of frequency for various groups of synthetic LFEs. Circles mark the coherence falloff frequencies: when P_c/P_l or P_d/P_l falls below 0.6. Inset panels show the moment rate functions averaged over LFEs in each group. Color indicates diameter (panel a), rupture velocity (panel c), and rise time (panel e). (b, d, f) Normalized coherence falloff frequencies $f_{fc}/(V_s/D)$ (filled circles) and $f_{fd}/(V_s/D)$ (open squares) as a function of the LFE properties. Color indicates the type of LFE rupture. Solid and dashed lines indicate approximations of the numerically identified f_{fc} and f_{fd} to be used in our interpretations. In panels a, b, c, and d, $t_r = 0.27D/V_r$. In panels a, b, e, and f, $V_r = 0.75V_s$. In panels c and e, $D = 456$ m. In panels d and f, the values plotted are medians taken from synthetics with 7 different diameters.

To consider the coherence's implications for LFE rupture areas, we need to know how P_d/P_l and P_c/P_l depend on LFE rupture properties. So we generate and analyze groups of synthetic LFEs with various diameters D, rupture velocities V_r, and rise times t_r. We create synthetic ruptures for three types of LFEs (section 6.1), analyze their waveforms (section 6.2), and examine the coherent frequencies as a function of the LFE properties (section 6.3).

6.1 Synthetic LFEs Models

We create and analyze groups of 100 LFEs. The individual events are assigned diameters D, rupture velocities V_r, and rise times t_r that cluster around specified mean values. The diameters, rupture velocities, and rise times are chosen from lognormal distributions with factor of 1.3, 1.1, and 1.3 standard deviations, respectively. Moments are chosen from lognormal distributions with factor of 1.5 standard deviation and assigned with no consideration of the radii.

In the simplest version of our LFEs, each event is assigned a random heterogeneous slip distribution within a roughly circular area, as detailed in section S4 and motivated by inferences of fractal earthquake slip distributions (*Frankel*, 1991; *Herrero and Bernard*, 1994; *Mai and Beroza*, 2002). Rupture initiates at a random location within $0.4D$ of the center and spreads radially at rate V_r. Once a location starts slipping, slip accumulates following a regularized Yoffe function with duration t_r (*Tinti et al.*, 2005).

We also construct groups of LFEs with more repetitive rupture patterns, as it is possible that LFEs within a given family recur not just on the same patch, but with similar rupture patterns within that patch (e.g., *Ariyoshi et al.*, 2009; *Ando et al.*, 2010; *Sweet et al.*, 2014; *Chestler and Creager*, 2017b). In our repetitive LFEs, slip is the sum of two heterogeneous distributions: one that varies randomly from event to event and one that is the same from event to event. The distributions are scaled so that the repetitive component contributes twice as much moment, and slip always nucleates within $0.1D$ of the LFE center points.

Finally, we construct groups of composite LFEs, as it is possible that individual LFEs comprise a series of small ruptures of the complex fault zone at depth (*Fagereng et al.*, 2014; *Hayman and Lavier*, 2014; *Chestler and Creager*, 2017b; *Rubin and Bostock*, 2017). Each of our relatively crude composite LFE contains five simple ruptures whose rupture velocities, diameters, and slip distributed are chosen from the lognormal and heterogeneous distributions described above. The five sub-ruptures begin at random times within a $2.5D/V_r$ interval.

6.2 Computing and Analyzing LFE Waveforms

Having defined the location and timing of slip in the LFEs, we compute ASTFs for nearby stations. We assume that the synthetic LFEs are in the location of family 37140 and calculate ASTFs for the 12 stations used in its analysis, as shown in Figures 2 and S1. To calculate ASTFs, we integrate the slip rate over the slipping area at each time step, but shift the signals' arrival times to account for the travel time from each point in the source region to the observing stations, as in equation (2). To calculate seismograms, we convolve these ASTFs with fake Green's functions, which are taken to be white noise tapered by an exponential with a 3-s decay constant.

We may now process the synthetic seismograms. As with the real data, we create templates for each LFE group, normalizing the synthetic seismograms by their maximum values and stacking. We iterate this stack three times. Each time, we cross-correlate the template seismograms with

the individual LFEs' waveforms. We identify a station-averaged time shift for each LFE, realign according to those shifts, and stack.

Next, we use the templates to compute the cross-spectrum $\hat{x}_{jk}$ for each synthetic LFE record (equation (4)). As with the real data, we compute the cross-spectra from the tapered cross-correlations, but we adjust the taper duration to ensure that it is always significantly longer than the LFEs' durations. Finally, we compute the LFEs' template-normalized powers P_c, P_d, and P_l (equations (5), (7), and (9)). Figure 5a, c, and e shows the coherent power fractions P_d/P_l and P_c/P_l obtained for simple LFEs with various diameters, rupture velocities, and rise times.

6.3 Coherence Falloff Frequencies as a Function of D, V_r, and t_r

6.3.1 Coherence Falloff with Diameter

As anticipated in section 2, both P_d/P_l and P_c/P_l decrease at lower frequencies (longer periods) when the LFE diameters are larger (panel a). P_d/P_l falls off earlier when diameters are larger because larger diameters imply longer ruptures, which allow for complexity and inter-LFE variability at lower frequencies. P_c/P_l falls off earlier because larger diameters imply larger shifts in the source-station travel time within the rupture area, and thus allow for inter-station ASTF variability at lower frequencies. To examine the coherence falloff systematically, we identify the frequencies at which P_d/P_l and P_c/P_l first fall below 0.6. These falloff frequencies f_{fd} and f_{fc} are normalized by V_s/D and plotted as a function of LFE diameter D in Figure 5b. In the simple LFE simulations in Figure 5b, which have $V_r/V_s = 0.75$ and $t_r = 0.27R/V_r$, f_{fd} is roughly $1.4V_s/D$ (open red squares and dashed red line), and f_{fc} is roughly $2.2V_s/D$ (filled red circles and solid red line).

Note that these ratios $f_{fd}/(V_s/D)$ and $f_{fc}/(V_s/D)$ could change slightly if we assumed a different distribution of stations, as different takeoff angles and azimuths could change the apparent source durations and travel time shifts. Here we have chosen a station distribution consistent with the stations used in analyzing the Parkfield data.

6.3.2 Coherence Falloff with Rupture Velocity

The direct coherence falloff frequency f_{fd} decreases relative to V_s/D if LFE rupture velocities are reduced, as shown Figure 5c and d. Note that when we plot $f_{fd}/(V_s/D)$ and $f_{fc}/(V_s/D)$ in Figure 5d and f, we take the median of estimates computed for 7 groups of LFEs, with different diameters, in order to reduce the scatter. The decrease of $f_{fd}/(V_s/D)$ with decreasing rupture velocities arises because lower rupture velocities allow for longer ruptures and therefore more complexity and inter-event variability at lower frequencies. The LFEs' heterogeneous slip distributions give rise to source time functions that differ among events at all frequencies shorter than the rupture duration, which scales as D/V_r in simulations of simple LFEs. The direct coherence falloff frequency f_{fd} thus scales inversely with the durations of these ruptures, with value around $2.8V_r/D$ when $V_r < 0.4V_s$, though it decreases relative to V_r/D for rupture velocities larger than $0.8V_s$ (red dashed line in Figure 5d).

The inter-station coherence falloff frequency f_{fc} depends more weakly on rupture velocity V_r. f_{fc} increases from 0.7 to $2.2V_s/D$ as V_r increases from 0.05 to $1V_s$ (filled red circles and solid red line in Figure 5d). P_c/P_l depends only weakly on V_r because P_c/P_l measures how much

the ASTFs vary among stations, not among events. The inter-station ASTF variability depends primarily on the S-wave travel time across the source region, which scales with D/V_s, not D/V_r. The V_r dependence that does exists likely results from the simpler ASTF pulses associated with higher rupture velocities. As V_r approaches V_s, the ASTFs tend toward single pulses, and inter-station complexity is harder to distinguish.

6.3.3 Coherence Falloff With Rise Time

Both f_{fd} and f_{fc} vary minimally in response to modest changes in the duration t_r of slip at each point in the rupture, especially when the rise time t_r is less than D/V_r (Figure 5c and f). In our implementation, we have assumed a spatially uniform rise time for each LFE. As a result, changing the rise time is roughly equivalent to convolving all of an LFE's ASTFs by a single function, and such a convolution has little effect on the inter-ASTF coherence. We do allow roughly 10% variability in rise time and rupture velocity among the LFEs in each group. These rise time differences, coupled with the increased complexity visible in longer-duration ruptures, are likely responsible for the reduced coherence falloff frequencies that become apparent once t_r exceeds 1 to $2D/V_r$. (red symbols and lines in Figure 5d).

6.3.4 LFE Durations

Increasing the rise time does increase LFE durations. To estimate durations for each LFE group, we stack the events' source time functions using the same alignment used in the stack creation. Then we identify the time interval containing the central 70% of the LFE moment. In our simple LFEs, these intervals have durations that increase from between 0.29 and $0.31D/V_r$ when t_r is $0.27D/V_r$ to roughly $0.28t_r$ as t_r gets longer than D/V_r. LFE durations are shorter when we require that LFEs nucleate near the rupture centers. For our modeled repetitive LFEs, which we assume nucleate within $0.1D$ of their center points, durations are 0.25 to $0.28D/V_r$ when t_r is $0.27D/V_r$. If we instead specify nucleation locations within $0.1D$ of the rupture edge, durations are 0.35 to $0.37D/V_r$. The durations of composite LFEs are determined by the number and timing of subevents. The presented LFEs, containing 5 subevents, have durations between 3 and $3.3D/V_r$.

6.3.5 Composite LFEs

The composite LFEs, with their long, complex ruptures, have reduced direct coherence. The direct coherence falloff frequency f_{fd} is around $0.25V_r/D$ for all simulated events (open blue squares and dashed lines in Figure 5b, d, and f). On the other hand, the inter-station falloff frequencies f_{fc} are similar for simple and composite LFEs (filled blue circles and solid blue line). Here again P_c/P_l depends primarily on D/V_s: on how much the source-station travel time can shift peaks in the source time functions.

6.3.6 Repetitive LFEs

The coherent power fractions P_d/P_l and P_c/P_l can be significantly higher for repetitive LFEs, at least when the rupture velocity is larger than about $0.5V_s$. As described in section 6.1, the repetitive LFEs in each group have similar slip distributions, and they all nucleate near the rupture center, so they have similar ASTFs and similar waveforms. This similarity explains the increase in

P_d/P_l, but the increase in P_c/P_l is surprising at first glance, as P_c/P_l measures similarity across stations, not across events. However, the cross-spectra calculation that goes into P_c (equation (4)) is designed to remove complexity associated with the path effects, and it identifies as "path effect" any component of the source-path convolution (equation (3)) that is common to all events. If the ASTFs are the same for all events, the P_c calculation cannot distinguish inter-station ASTF variations from station-dependent Green's functions, ASTF variations are thus attributed to path effects, and P_c/P_l is high when LFEs are highly repetitive. The falloff frequencies f_{fc} can increase by a factor of 6 when $V_r > 0.8V_s$.

We note, however, that this factor of 6 increase in f_{fc} is just one plausible value. Here we have assumed that two-thirds of the LFE moment came from a repetitive component of the rupture, but higher or lower coherence could be achieved by assuming that more or less of the moment came from the repetitive component. We also note that the high coherence arises only when the rupture nucleation location is consistent from event to event. The falloff frequencies f_{fc} remain low if only 75% of the repetitive LFEs nucleate at the SE rupture edge and the other 25% nucleate on the NW edge (Figure S22).

7 Interpretation of LFE Coherence

We may now use our synthetic results to interpret the coherence obtained for the Parkfield LFE families, which show direct coherence $P_d/P_l > 0.5$ out to 4 to 5 Hz and inter-station coherence $P_c/P_l > 0.5$ out to 8 to 16.5 Hz.

7.1 LFE Location Distribution

First, we note that the observed high-frequency coherence implies that LFEs within each family are strongly clustered in space. If LFEs were distributed over a wide range of locations, travel times from the LFE centroids to the recording stations would vary widely from event to event. But in our analysis, we allow only the origin time to be realigned from event to event. Any inter-station time shifts produced by varying LFE locations should show up in our results as a decrease in coherence.

To determine the maximum location variation allowed by the observations, we recompute coherence values after artificially shifting the LFE locations by various amounts. We pick location shifts for each LFE in family 37140, drawing from bivariate normal distributions with 100-m to 1-km standard deviations along strike and depth. We use the IASP91 velocity model and TauP to compute the arrival time change for the stations observing each LFE (*Kennett and Engdahl*, 1991; *Crotwell et al.*, 1999). We subtract the median arrival time change from these values, shift the seismograms by the station-dependent remainders, and compute the coherent power fractions. The family-averaged results are shown in Figures 6 and S15-S17. We find that the inter-station coherent fraction P_c/P_l obtained at 11 Hz is reduced by 40% even for location shifts with just 250-m standard deviation (Figure 6). The > 0.6 11-Hz coherence values obtained for the median family thus imply that LFEs in each family are strongly clustered, with standard deviation in their locations typically smaller than 250 m.

Note that the distribution of LFE locations within a family, when coupled with noise, is one way to explain all of the incoherence observed at higher frequencies in the data. It is possible that

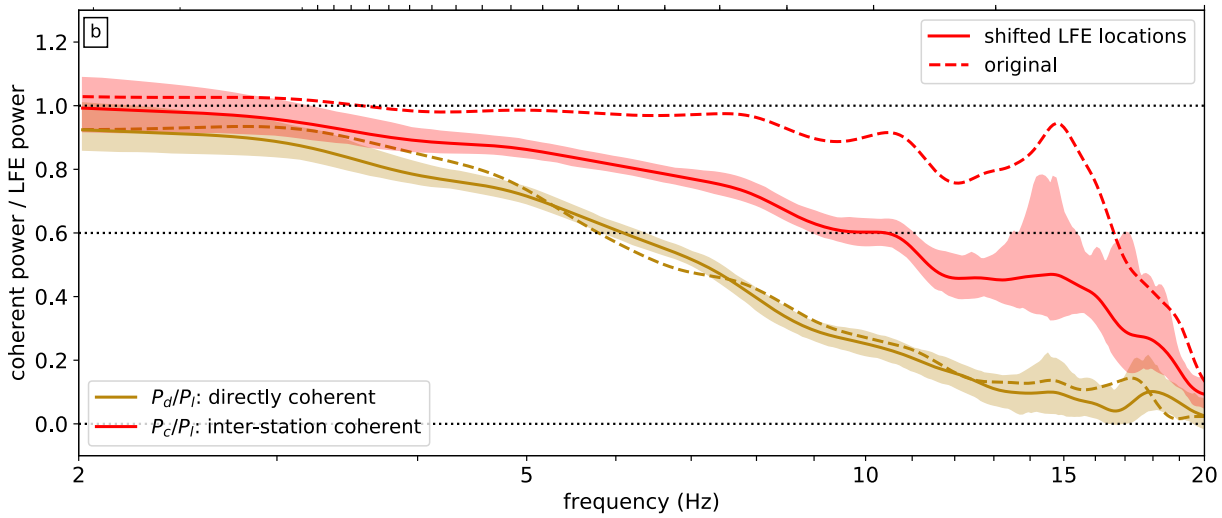

Figure 6: Solid lines and shading: coherent power fractions for family 37140, as in Figure 4b, but computed after shifting the LFE locations by random amounts with 250-m standard deviations along strike and along depth. Dashed lines: original P_d/P_l and P_c/P_l, without location shifts, reproduced from Figure 4b.

the individual LFEs appear to be point sources—that each LFE ruptures a tiny patch within the sub-1-km asperity (*Chestler and Creager*, 2017a).

7.2 Matching f_{fc}, f_{fd}, and Duration With Simple Ruptures: Results

However, it is also possible that the finite rupture areas of individual LFEs contribute to the decrease in coherence at high frequencies. To determine the maximum rupture areas and rupture velocities allowed by the data, we compare the observed coherence falloff frequencies and durations with those obtained from synthetics of simple, non-repetitive ruptures.

First, we note that the inter-station coherence P_c/P_l remains higher than 0.6 out to 8 to 16.5 Hz for the various families. The median P_c/P_l falloff frequency f_{fc} is 11 Hz, and families 37102 and 37140, which we will discuss in more detail, have f_{fc} of 9 and 16.5 Hz, respectively. In the synthetics, f_{fc} is 0.7 to $2.2V_s/D$ for rupture velocities V_r between 0.05 and $1V_s$ (red solid line in Figure 5d). If the shear wave velocity V_s is around 4 km/s in the LFE area (*Lin et al.*, 2010), family 37102's 9-Hz f_{fc} implies an average diameter smaller than 300 to 1000 m, with smaller allowable diameters for slower rupture velocities. In Figure 7a, this range of allowable diameters is marked with blue diagonal hatching. The thicker blue line presents alternative upper bound on the diameter, ranging from 180 to 550 m. It is appropriate for a 16-Hz f_{fc}: the bootstrap-estimated lower bound on f_{fc} obtained for family 37140.

The yellow diagonal hatching in Figure 7a illustrates a further, albeit weaker, constraint on the LFEs' diameters and rupture velocities: those obtained from the direct coherence P_d/P_l. P_d/P_l is higher than 0.6 out to 4 to 5 Hz for all seven LFE families, though it could be biased high or low by uncertainties in the LFE origin time alignment (see Appendix A1). In the synthetics, the P_d/P_l falloff frequency f_{fd} scales roughly with 1 over duration. It ranges from 1.4 to $2.8V_r/D$,

or from 0.15 to $1.4V_s/D$ (blue dashed line in Figure 5d). Coupling the synthetics with a 5-Hz f_{fd} constrains the LFE diameters to be less than 1100 m.

More important constraints on the LFE properties come from the LFE durations estimated by *Thomas et al.* (2016). *Thomas et al.* (2016) compared LFE stacks with nearby earthquakes' waveforms and obtained best-fitting durations of 0.19 and 0.22s for LFEs in families 37140 and 37102, respectively. To get a sense of the uncertainty, we note that their best fits come from averaging over comparisons with 12 or 17 different local earthquakes, but they also present the durations obtained by the individual earthquake comparisons. Only one earthquake comparison gives a family 37140 duration smaller than 0.15 or larger than 0.22, and only one comparison gives a family 37102 duration smaller than 0.15 or larger than 0.3, so we use these values as uncertainty bounds. To compare the durations to our synthetics, we note that 70% of the moment in the stacked synthetic LFEs accumulates within 0.29 to $0.31V_r/D$. *Thomas et al.* (2016) modeled the LFE waveforms with a Hann-like source time function, which accumulates 70% of its moment within 40% of length, so the 70% durations for families 37140 and 37102 are 0.060 to 0.087 and 0.060 to 0.12 s, respectively. We multiply these 70% durations by 1.4 to $2.8V_r$ to estimate LFE diameters and plot the results with red vertical hatching in Figure 7a. The lower and upper thick red lines mark the diameters expected for the best-fitting durations for families 37140 and 37102, respectively.

The diameters implied by the observed durations match those implied by family 37102's $>$ 9 Hz f_{fc} for a wide range of rupture velocities. The two sets of constraints overlap at least partially for all plotted V_r/V_s, and the inter-station coherence constraint matches the median duration when $V_r < V_s$. According to these results, LFEs in family 37102 could be slow ruptures, with 200-m diameters and $V_r = 0.2V_s$. Or they could be relatively "normal" earthquakes, with 800-m diameters and $V_r = 0.8V_s$. Note that changing the assumed shear wave velocity V_s would change the estimated diameters in Figure 7, but not the V_r/V_s intersection ranges, as all of the plotted diameter constraints scale with $1/V_s$.

Given the uncertainties in the data, the constraints on LFEs in family 37140 could also be matched with a range of rupture speeds. This family's $f_{fc} \gtrsim 16$ Hz constraint (below the solid blue line) starts to intersect the duration constraints when $V_r < 0.7V_s$. However, we should note that the plotted 16-Hz constraint is already the 95% lower bound on f_{fc}, obtained from bootstrapping. The best-fitting f_{fc} is 16.5 Hz. Further, the $f_{fc} \gtrsim 16$ Hz constraint intersects the best-fitting duration only when $V_r < 0.4V_s$. Family 37140's data are thus best matched when $V_r < 0.4V_s$.

7.3 Matching f_{fc}, f_{fd}, and Duration With Simple Ruptures: Uncertainties

To further assess whether earthquake-like rupture velocities V_r of 0.7 to $0.9V_s$ are plausible, not just possible, for family 37140, we consider additional sources of uncertainty in the duration- and coherence-derived diameters. The diameters implied by the durations would decrease slightly if all ruptures began at the asperity edge. Groups of synthetic ruptures starting within $0.1D$ of the LFE edge have durations of 0.35 to $0.37D/V_r$, rather than the 0.29 to $0.31D/V_r$ values estimated for events starting within $0.4D$ of the center. However, synthetic ruptures starting from the edge also give f_{fc} values about 20% smaller than those starting closer to the center (Figure S19). Changing both constraints leaves the range of allowable rupture velocities almost unchanged.

Other minor modifications to the rupture parameters appear to affect the f_{fc} constraints minimally. For instance, we observe little change in f_{fc} if we add a smooth tapered component to

the heterogeneous slip distributions (Figure S21) or if we limit the range of diameters within each group to a factor of 1.1 standard deviation (Figure S23). However, we have not explored the entire range of rupture parameters. Perhaps we would obtain higher coherence if we made the slip distribution and temporal evolution smoother or slightly more repetitive, more similar to the repeater-like LFEs discussed in sections 6.1 and 7.4.

Another scenario that seems unlikely but possible is that the 16.5-Hz f_{fc} obtained for family 37140 reflects random variability. This f_{fc} is significantly larger than the median f_{fc} for the seven families, which is just 11-Hz, and the synthetics in Figure 5b do show tens of percent variability in f_{fc} among LFE groups, simply as a result of random variations in the slip distributions. However, those synthetics use only 100 LFEs. Using several thousand should reduce the uncertainty. Further, bootstrapping events within each synthetic group gives a reasonable estimate of the variability among the groups. Bootstrapping the data in family 37140 gives 95% probability that $f_{fc} > 16$ Hz.

The other uncertainties in the data, along with potential variation in LFE location, would imply that the estimated 16.5-Hz f_{fc} is a lower bound on the true value, as discussed in section 5 and appendix A1. Given these uncertainties, we cannot exclude the possibility that these LFEs are simple ruptures with "typical" earthquake rupture speeds around $0.7V_s$. But we consider it more likely that the rupture velocities are lower than $0.7V_s$. The data are best matched by simple LFEs when rupture velocities are less than $0.4V_s$.

7.4 Matching the Data With Modified LFE Ruptures

It is also possible to match the data if we modify the LFE dynamics significantly: if LFEs are composite ruptures, ruptures with long rise times, or repetitive ruptures, as described in section 6.1. Figure 7b-d illustrate the constraints obtained for some plausible rupture parameters.

Figure 7b illustrates the constraints on diameters and rupture velocity if LFEs are composed of 5 sub-ruptures distributed over an interval with duration $2.5D/V_r$. Here the inter-station coherence constraints (blue) are essentially unchanged, but the direct coherence and duration constraints imply smaller diameters.

Figure 7c illustrates the constraints if LFEs have rise times equal to $5D/V_r$. In these LFEs, rupture would progress to the asperity edge, and then the whole patch would continue slipping together.

Finally, Figure 7d illustrates the constraints on D and V_r/V_s if LFEs are repetitive ruptures, which persistently nucleate in the same region, and which have two-thirds of their moment is associated with a slip distribution that is consistent from event to event. With these repetitive ruptures, the 16-Hz f_{fc} of family 37140 can be matched even if the rupture diameters are larger.

A wide range of parameters could also match the data if LFE durations are actually reflections of local attenuation, not the LFE source dynamics (*Gomberg et al.*, 2012; *Bostock et al.*, 2017). In this case, the diameters estimated from the durations (red lines) are upper bounds, and the data can be matched by any combination of rupture velocity and diameter that plots below those bounds and within the f_{fc} (blue) and f_{fd} (red) constraints.

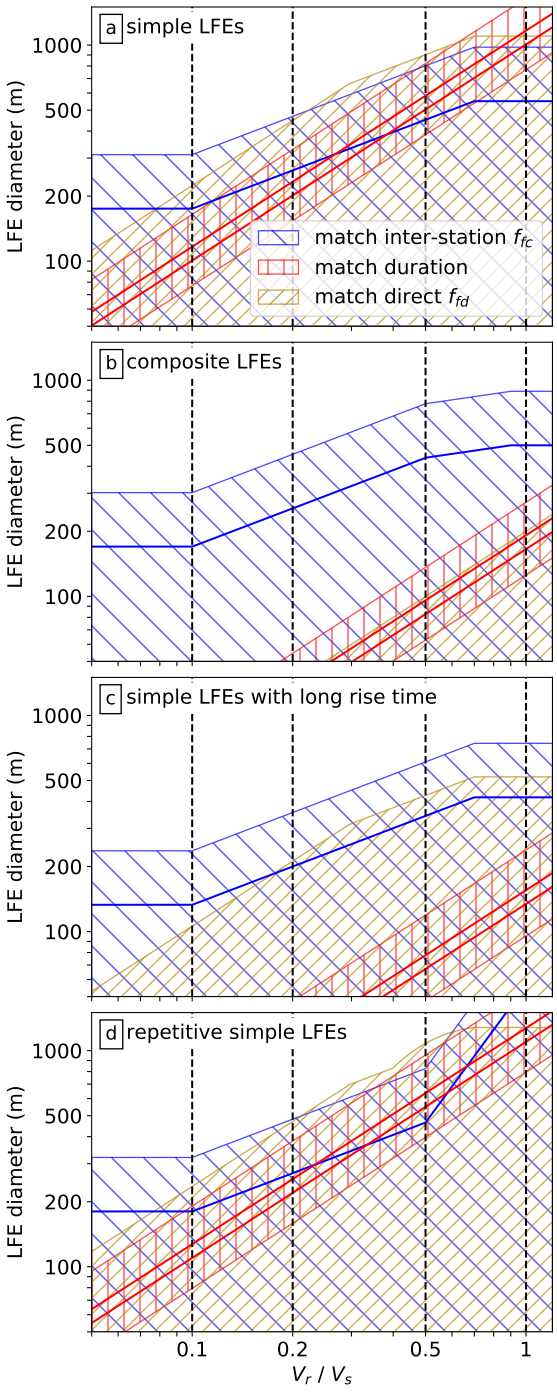

Figure 7: Hatched regions mark diameters (y-axis) and rupture velocities (x-axis) that match each of the 3 observations: f_{fc} (blue diagonal lines), f_{fd} (yellow diagonal lines), and the durations of *Thomas et al.* (2016) (red vertical lines). The four panels are for four approaches to constructing the LFEs, as indicated by the text in the upper left.

8 Discussion

8.1 Implications for Tremor Asperities

Regardless of the individual LFE rupture dynamics, our observations of high-frequency coherence suggest that LFEs are clustered in patches less than 1 km across. As noted in the introduction, such clustering has also been inferred by careful analysis of LFE families in Cascadia (*Sweet et al.*, 2014; *Chestler and Creager*, 2017a) and may be suggested by highly periodic LFE ruptures in Parkfield (*Shelly*, 2010b). The clustering may suggest a role for material heterogeneity in controlling the occurrence of tremor. It is consistent with proposals that tremor's LFEs rupture a collection of unstable asperities embedded in a larger, more stable region (*Ando et al.*, 2010; *Nakata et al.*, 2011; *Ando et al.*, 2012; *Ariyoshi et al.*, 2012; *Veedu and Barbot*, 2016; *Luo and Ampuero*, 2017). Larger asperities may also exist, as patches of tremor are observed on scales of a few to tens of km. The larger tremor patches could represent groups of tremor asperities or regions more prone to distributed rapid slip (*Shelly*, 2010b; *Ghosh et al.*, 2012; *Armbruster et al.*, 2014; *Yabe and Ide*, 2014; *Savard and Bostock*, 2015; *Annoura et al.*, 2016; *Kano et al.*, 2018). Alternatively, the large and small tremor patches could represent persistent slip patterns that have arisen on a simple, homogeneous fault. Such patterns are sometimes seen in models that lack heterogeneity in material properties (*Horowitz and Ruina*, 1989; *Langer et al.*, 1996; *Shaw and Rice*, 2000), though it remains to be assessed whether these models can produce clusters of tremor that persist over many slow slip cycles, as we observe in Parkfield.

The family-based clustering implied by our coherence estimates and by others' LFE relocations (*Sweet et al.*, 2014; *Chestler and Creager*, 2017a) suggests that cross-correlation based LFE families are more an observational convenience (*Shelly et al.*, 2007; *Brown et al.*, 2008; *Bostock et al.*, 2012; *Frank et al.*, 2013; *Kato*, 2017; *Shelly*, 2017). The analyzed families show sub-km LFE clustering even though some are separated from neighboring families by a few to 5 km. The LFEs' tendency to occur on these asperities lends further confidence to studies that have interpreted LFE repeat rates as indicators of the slip rate in a creeping area surrounding the more unstable LFE patches (*Rubin and Armbruster*, 2013; *Royer et al.*, 2015; *Lengliné et al.*, 2017; *Thomas et al.*, 2018).

8.2 Implications for Tremor Physics

Given our observations and synthetics of LFE coherence as a function of rupture diameter, there are still several ways to explain the long, 0.2-s durations of Parkfield LFEs. First, it is possible that families 37102 and 37140's LFEs are normal earthquakes with near-shear-wave rupture speeds. A $0.7V_s$ rupture speed is at the edge of the constraints for family 37140, but such rapid ruptures could match the data better if the LFEs are somewhat repetitive, with nucleation locations and slip distributions that persist from event to event. And a wide range of high rupture speeds could match the data if the 0.2-s durations we use are overestimates of the true durations, despite *Thomas et al.* (2016)'s careful empirical Green's function analysis. The durations could be overestimated if a highly attenuating region is localized around the LFE patches, so that attenuation removes the high-frequency components of the LFE seismograms but has little effect on the seismograms of the reference earthquakes, which are located a few km away.

If LFEs do have durations of 0.2 s and rupture speeds up to $0.7V_s$, they could have diameters

up to 800 m. Uniform stress drop M_w 1 to 2 earthquakes with 800-m diameters would have stress drops of 0.3 to 9 kPa and average slips of 0.002 to 0.06 mm (*Eshelby*, 1957; *Shearer*, 2009). These moment and slip estimates are imprecise, and difficult to estimate because LFE locations are offset from local earthquakes, but we note that if the larger slip estimates are representative, almost all of the slip on the LFE patch could be seismic. Even 800-m-wide LFEs could accommodate most of the long-term slip on the LFE patch, which *Thomas et al.* (2016) estimated to be around 0.05 mm per event.

But while LFEs from both families can be matched by rupture velocities up to $0.7V_s$, the data from family 37140 are better matched by LFEs with slower rupture speeds ($< 0.4V_s$), long rise times, or a composite of subevents. Any of these scenarios would have interesting implications for the physics of LFE ruptures. For instance, rupture speeds around $0.4V_s$, which can match the data for both families, would suggest that the LFEs' radiation efficiency is around 0.5: that about half of the energy in LFEs is released via seismic wave generation, with the rest expended as fracture energy (e.g., *Kostrov*, 1966; *Eshelby*, 1969; *Fossum and Freund*, 1975; *Venkataraman and Kanamori*, 2004; *Kanamori and Rivera*, 2006). Such low but significant radiation efficiency *could* mean that LFEs are exceptionally weak but otherwise normal earthquakes. LFEs may be driven by unstable frictional sliding, and their slip rates may be limited by the dissipation of energy via seismic waves. Although $0.4V_s$ is lower than typical earthquake rupture speeds (*McGuire*, 2004; *Seekins and Boatwright*, 2010; *Folesky et al.*, 2016; *Ye et al.*, 2016; *Melgar and Hayes*, 2017; *Chounet et al.*, 2018), such speeds are sometimes observed in earthquakes, especially in shallow tsunami earthquakes (e.g., *Ide et al.*, 1993; *Ihmlé et al.*, 1998; *Venkataraman and Kanamori*, 2004; *Bilek and Engdahl*, 2007; *Polet and Kanamori*, 2009; *Cesca et al.*, 2011).

It is thus possible that LFEs are simply earthquakes driven by a frictional weakening process that is for some reason smaller in magnitude than the processes driving normal earthquakes. LFEs might nucleate "earlier" than most earthquakes, at times when there is only a modest stress drop available to drive rupture. Or LFEs could nucleate on small unstable patches but then move quickly into regions that resist high slip speeds, perhaps because they are velocity-strengthening or allow for large off-fault deformation. Such acceleration-resisting regions have been suggested to limit the rupture velocities of tsunami earthquakes (e.g., *Bilek and Lay*, 2002; *Faulkner et al.*, 2011a; *Ma*, 2012). Off-fault deformation seems an appealing process to invoke for tremor because complex brittle and ductile deformation is observed at relevant depths (*Fusseis et al.*, 2006; *Handy et al.*, 2007; *Collettini et al.*, 2011; *Fagereng et al.*, 2014; *Hayman and Lavier*, 2014; *Angiboust et al.*, 2015; *Behr et al.*, 2018; *Webber et al.*, 2018). It is even possible that each LFE is a collection of small brittle failures, rupturing small faults or veins (*Fagereng et al.*, 2014; *Ujiie et al.*, 2018). However, it remains unclear how or if that distributed ductile deformation would limit the rupture speeds of LFEs. Off-fault ductile deformation can also accumulate in large earthquakes, with near-shear-wave rupture speeds (*DeDontney et al.*, 2011; *Dunham et al.*, 2011; *Roten et al.*, 2017).

Another possibility is that LFEs do rupture at near-shear-wave speeds, but that the shear wave speed is significantly reduced in the LFE area because of lithological variations, fault zone damage, or high pore pressures (*Audet et al.*, 2009; *Song et al.*, 2009; *Kato et al.*, 2010; *Fagereng and Diener*, 2011; *Stefano et al.*, 2011; *Huang et al.*, 2014). Fault damage zones are frequently observed at a range of depths (*Shipton and Cowie*, 2001; *Rowe et al.*, 2009; *Faulkner et al.*, 2011b; *Rempe et al.*, 2013; *Leclère et al.*, 2015), and they sometimes show 30 to 50% reductions in wavespeed, at least in shallow regions (*Ben-Zion et al.*, 2003; *Cochran et al.*, 2009; *Lewis and Ben-Zion*, 2010; *Yang et al.*, 2014; *Li et al.*, 2016). It is difficult to fully assess a low-wavespeed region's implica-

tions for our observations. The inter-station coherence we observe depends on the seismic waves' source-station travel times, and those times depend on which source-station paths are traveled. But in the simplest case, where LFE signals begin by traveling horizontally away from the fault, so that they move outside the fault zone before continuing to the surface, the travel time variation we probe with inter-station coherence would depend primarily on the higher wavespeed outside the fault zone. The higher wavespeeds could allow for the high-frequency inter-station coherence we observe even though the lower wave speed inside the fault zone limits the rupture velocity and produces long-duration events.

On the other hand, it is possible that LFE rupture velocities are not limited by seismic wave radiation at all, but by a different fault zone rheology. We note that the results from family 37140 are best fit by simple LFE ruptures with $V_r < 0.4V_s$, and because of noise in the data, all of our coherence-constrained diameters and rupture speeds are upper bounds on the true values. So LFE rupture speeds could be much smaller: $0.2V_s$, for example. Such slowly rupturing LFEs would release more than 80% of their energy via fracture energy, making it unlikely that the energy dissipated via seismic wave radiation could limit the slip speeds. The low rupture velocities inferred for family 37140 could be telling us that LFE rupture dynamics are controlled by a different deformation mechanism than normal earthquakes—perhaps by the same speed-limiting rheology that controls slow slip events (e.g., *Ide et al.*, 2007; *Shibazaki and Iio*, 2003; *Shibazaki and Shimamoto*, 2007; *Ide et al.*, 2008; *Aguiar et al.*, 2009; *Liu et al.*, 2010; *Segall et al.*, 2010; *Gao et al.*, 2012; *Hawthorne and Rubin*, 2013; *Ide and Yabe*, 2014; *Hawthorne and Bartlow*, 2018).

9 Conclusions

We have analyzed inter-station and inter-event coherence between LFEs in seven families near Parkfield, CA. Our synthetic analysis shows that we can use inter-station ASTF variations to estimate LFE or earthquake rupture areas. Our observations of LFE coherence imply that LFEs in each family are strongly clustered, with standard deviation in their locations smaller than 250 m. Comparing the observed coherence with that of synthetic LFE ruptures implies that the LFE diameters are smaller than 500 to 1100 m, depending on the family. Coupling the coherence constraints with the LFE durations estimated by *Thomas et al.* (2016) suggests that we could match the data for LFEs in family 37102 with a wide range of rupture models, including earthquake-like ruptures with rupture velocities V_r of 0.7 to 0.9 times the shear wave speed V_s. For family 37140, $V_r = 0.7V_s$ can match the data, but only on the edge of the constraints, and the data are better matched with $V_r < 0.4V_s$. Such low rupture speeds may indicate that LFEs are governed by a slow slip rheology, not by standard unstable frictional sliding, but we note that data from both families of LFEs could also be matched if LFEs are repetitive fast ruptures, composite ruptures, or ruptures with long rise times. Our synthetics illustrate how the coherence and durations might differ among these rupture types, and thus how we might probe the physics of LFEs with future observations.

Acknowledgments

We also used seismic waveform data from the Berkeley Parkfield High Resolution Seismic Network (HRSN), provided via the Northern California Earthquake Data Center and the Berkeley

Seismological Laboratory (doi: 10.7932/NCEDC), as well as seismic waveform data from the Plate Boundary Observatory (PBO) borehole seismic network, operated by UNAVCO and funded by NSF grant EAR-0732947. The PBO data was obtained via IRIS. The fault traces shown in Figure 2 were obtained from the USGS and California Geological Survey fault and fold database, accessed from http://earthquake.usgs.gov/hazards/qfaults in 2016.

A1 Decoherence from Noise

Our coherence frequencies should probably be interpreted as lower bounds, as several sources of noise could reduce the observed P_d/P_l and P_c/P_l from their true values. First, decreased P_d/P_l and P_c/P_l could arise if a significant portion of the "noise" comes from LFEs that are nearby but not in the family of interest. LFEs are clustered in space and time (e.g., *Shelly*, 2010a; *Bostock et al.*, 2015) so the noise from other LFEs may be higher during the LFE window than during the noise window before it. We estimate the noise power P_n in a window that starts just 8 s before the LFE S arrival to minimize the potential difference, but we cannot account for sub-8 s clustering. Note that in principle our noise window could include some of the P arrival. However, we find the P arrival is too late and too small to significantly affect the P_n estimates. Truncating the noise waveforms before the P arrivals and reprocessing changes our results negligibly.

Decreased P_d/P_l and P_c/P_l could also result from noise in the template LFEs. The template signals start to become poorly resolved at frequencies higher than 15 Hz, so it is difficult to calculate robust powers at those frequencies.

Finally, decreased or increased P_d/P_l could result from uncertainty in the LFE origin time. To accurately calculate direct coherence at high frequencies, we need well aligned waveforms, so we re-compute LFE origin times using 0.01-s precision. The realignment affects P_c/P_l negligibly but increases the frequencies with $P_d/P_l > 0.5$ by several Hz relative to results without recomputed origin time. One might worry that the increase in coherence comes from aligning the template with coherent noise rather than with LFE signal. However, we require at least 5 stations for the power estimates for each LFE, and we allow only one origin time shift per LFE. Assuming noise is random among stations, realigning with noise should increase P_d/P_l by less than 0.2.

The LFE detection approach of *Shelly* (2017) could also result in slightly increased coherence if noise contributes a part of the identified coherent signals. Finally, slightly increased coherence could result from our exclusion of signals with especially high noise. Note that the detected-facilitated increases in coherence are most likely to occur at low frequencies, around a few Hz, as these frequencies contribute most of the seismogram power involved in LFE selection and alignment.

There are no other obvious sources of artificially high coherence. Applying our processing to noise intervals rather than LFEs gives P_c/P_l and P_d/P_l of 0.01 or less.

References

Aguiar, A. C., T. I. Melbourne, and C. W. Scrivner, Moment release rate of Cascadia tremor constrained by GPS, *J. Geophys. Res.*, *114*, B00A05, doi:10.1029/2008JB005909, 2009.

Ando, R., R. Nakata, and T. Hori, A slip pulse model with fault heterogeneity for low-frequency earthquakes and tremor along plate interfaces, *Geophys. Res. Lett.*, *37*, L10310, doi:10.1029/2010GL043056, 2010.

Ando, R., N. Takeda, and T. Yamashita, Propagation dynamics of seismic and aseismic slip governed by fault heterogeneity and Newtonian rheology, *J. Geophys. Res.*, *117*(B11), B11308, doi:10.1029/2012JB009532, 2012.

Angiboust, S., J. Kirsch, O. Oncken, J. Glodny, P. Monié, and E. Rybacki, Probing the transition between seismically coupled and decoupled segments along an ancient subduction interface, *Geochem., Geophys., Geosyst.*, *16*(6), 1905–1922, doi:10.1002/2015GC005776, 2015.

Annoura, S., K. Obara, and T. Maeda, Total energy of deep low-frequency tremor in the Nankai subduction zone, southwest Japan, *Geophys. Res. Lett.*, *43*(6), 2562–2567, doi:10.1002/2016GL067780, 2016.

Ariyoshi, K., T. Hori, J.-P. Ampuero, Y. Kaneda, T. Matsuzawa, R. Hino, and A. Hasegawa, Influence of interaction between small asperities on various types of slow earthquakes in a 3-D simulation for a subduction plate boundary, *Gondwana Res.*, *16*(3-4), 534–544, doi:10.1016/j.gr.2009.03.006, 2009.

Ariyoshi, K., T. Matsuzawa, J.-P. Ampuero, R. Nakata, T. Hori, Y. Kaneda, R. Hino, and A. Hasegawa, Migration process of very low-frequency events based on a chain-reaction model and its application to the detection of preseismic slip for megathrust earthquakes, *Earth Planets Space*, *64*(8), 693–702, doi:10.5047/eps.2010.09.003, 2012.

Armbruster, J. G., W.-Y. Kim, and A. M. Rubin, Accurate tremor locations from coherent S and P waves, *J. Geophys. Res.*, *119*(6), 5000–5013, doi:10.1002/2014JB011133, 2014.

Audet, P., and A. J. Schaeffer, Fluid pressure and shear zone development over the locked to slow slip region in Cascadia, *Science Advances*, *4*(3), eaar2982, doi:10.1126/sciadv.aar2982, 2018.

Audet, P., M. G. Bostock, N. I. Christensen, and S. M. Peacock, Seismic evidence for overpressured subducted oceanic crust and megathrust fault sealing, *Nature*, *457*, 76–78, doi:10.1038/nature07650, 2009.

Baltay, A., G. Prieto, and G. C. Beroza, Radiated seismic energy from coda measurements and no scaling in apparent stress with seismic moment, *J. Geophys. Res.*, *115*, B08314, doi:201010.1029/2009JB006736, 2010.

Behr, W. M., A. J. Kotowski, and K. T. Ashley, Dehydration-induced rheological heterogeneity and the deep tremor source in warm subduction zones, *Geology*, *46*(5), 475–478, doi:10.1130/G40105.1, 2018.

Bell, R., R. Sutherland, D. H. N. Barker, S. Henrys, S. Bannister, L. Wallace, and J. Beavan, Seismic reflection character of the Hikurangi subduction interface, New Zealand, in the region of repeated Gisborne slow slip events, *Geophys. J. Intern.*, *180*(1), 34–48, doi:10.1111/j.1365-246X.2009.04401.x, 2010.

Ben-Zion, Y., Z. Peng, D. Okaya, L. Seeber, J. G. Armbruster, N. Ozer, A. J. Michael, S. Baris, and M. Aktar, A shallow fault-zone structure illuminated by trapped waves in the Karadere–Duzce branch of the North Anatolian Fault, western Turkey, *Geophys. J. Intern.*, *152*(3), 699–717, doi:10.1046/j.1365-246X.2003.01870.x, 2003.

Bilek, S. L., and E. R. Engdahl, Rupture characterization and aftershock relocations for the 1994 and 2006 tsunami earthquakes in the Java subduction zone, *Geophys. Res. Lett.*, *34*(20), doi:10.1029/2007GL031357, 2007.

Bilek, S. L., and T. Lay, Tsunami earthquakes possibly widespread manifestations of frictional conditional stability, *Geophys. Res. Lett.*, *29*(14), 1–4, doi:10.1029/2002GL015215, 2002.

Bostock, M. G., A. A. Royer, E. H. Hearn, and S. M. Peacock, Low frequency earthquakes below southern Vancouver Island, *Geochem., Geophys., Geosyst.*, *13*(11), Q11007, doi:10.1029/2012GC004391, 2012.

Bostock, M. G., A. M. Thomas, G. Savard, L. Chuang, and A. M. Rubin, Magnitudes and moment-duration scaling of low-frequency earthquakes beneath southern Vancouver Island, *J. Geophys. Res.*, *120*(9), 6329–6350, doi:10.1002/2015JB012195, 2015.

Bostock, M. G., A. M. Thomas, A. M. Rubin, and N. I. Christensen, On corner frequencies, attenuation, and low-frequency earthquakes, *J. Geophys. Res.*, *122*(1), 543–557, doi:10.1002/2016JB013405, 2017.

Brown, J. R., G. C. Beroza, and D. R. Shelly, An autocorrelation method to detect low frequency earthquakes within tremor, *Geophys. Res. Lett.*, *35*(16), L16305, doi:10.1029/2008GL034560, 2008.

Brown, J. R., G. C. Beroza, S. Ide, K. Ohta, D. R. Shelly, S. Y. Schwartz, W. Rabbel, M. Thorwart, and H. Kao, Deep low-frequency earthquakes in tremor localize to the plate interface in multiple subduction zones, *Geophys. Res. Lett.*, *36*, L19306, doi:10.1029/2009GL040027, 2009.

Cesca, S., T. Dahm, C. Juretzek, and D. Kühn, Rupture process of the 2001 May 7 Mw 4.3 Ekofisk induced earthquake, *Geophys. J. Intern.*, *187*(1), 407–413, doi:10.1111/j.1365-246X.2011.05151.x, 2011.

Chamberlain, C. J., D. R. Shelly, J. Townend, and T. A. Stern, Low-frequency earthquakes reveal punctuated slow slip on the deep extent of the Alpine Fault, New Zealand, *Geochem., Geophys., Geosyst.*, *15*(7), 2984–2999, doi:10.1002/2014GC005436, 2014.

Chestler, S. R., and K. C. Creager, Evidence for a scale-limited low-frequency earthquake source process, *J. Geophys. Res.*, *122*(4), 3099–3114, doi:10.1002/2016JB013717, 2017a.

Chestler, S. R., and K. C. Creager, A model for low-frequency earthquake slip, *Geochem., Geophys., Geosyst.*, *18*(12), 4690–4708, doi:10.1002/2017GC007253, 2017b.

Chounet, A., M. Vallée, M. Causse, and F. Courboulex, Global catalog of earthquake rupture velocities shows anticorrelation between stress drop and rupture velocity, *Tectonophysics*, *733*, 148–158, doi:10.1016/j.tecto.2017.11.005, 2018.

Cochran, E. S., Y.-G. Li, P. M. Shearer, S. Barbot, Y. Fialko, and J. E. Vidale, Seismic and geodetic evidence for extensive, long-lived fault damage zones, *Geology*, *37*(4), 315–318, doi: 10.1130/G25306A.1, 2009.

Collettini, C., A. Niemeijer, C. Viti, S. A. Smith, and C. Marone, Fault structure, frictional properties and mixed-mode fault slip behavior, *Earth Planet. Sci. Lett.*, *311*(3–4), 316–327, doi: 10.1016/j.epsl.2011.09.020, 2011.

Crotwell, H. P., T. J. Owens, and J. Ritsema, The TauP toolkit: flexible seismic travel-time and ray-path utilities, *Seis. Res. Lett.*, *70*(2), 154–160, doi:10.1785/gssrl.70.2.154, 1999.

DeDontney, N., E. L. Templeton-Barrett, J. R. Rice, and R. Dmowska, Influence of plastic deformation on bimaterial fault rupture directivity, *J. Geophys. Res.*, *116*(B10), B10312, doi: 10.1029/2011JB008417, 2011.

Dunham, E. M., D. Belanger, L. Cong, and J. E. Kozdon, Earthquake ruptures with strongly rate-weakening friction and off-fault plasticity, Part 1: Planar faults, *Bull. Seis. Soc. Amer.*, *101*(5), 2296–2307, doi:10.1785/0120100075, 2011.

Eshelby, J. D., The determination of the elastic field of an ellipsoidal inclusion, and related problems, *Proc. Roy. Soc. London. Series A. Mathematical and Physical Sciences*, *241*(1226), 376–396, doi:10.1098/rspa.1957.0133, 1957.

Eshelby, J. D., The elastic field of a crack extending non-uniformly under general anti-plane loading, *Journal of the Mechanics and Physics of Solids*, *17*(3), 177–199, doi:16/0022-5096(69)90032-5, 1969.

Fagereng, Å., and J. F. A. Diener, San Andreas Fault tremor and retrograde metamorphism, *Geophys. Res. Lett.*, *38*(23), L23303, doi:10.1029/2011GL049550, 2011.

Fagereng, Å., G. W. B. Hillary, and J. F. A. Diener, Brittle-viscous deformation, slow slip, and tremor, *Geophys. Res. Lett.*, *41*(12), 4159–4167, doi:10.1002/2014GL060433, 2014.

Faulkner, D. R., T. M. Mitchell, J. Behnsen, T. Hirose, and T. Shimamoto, Stuck in the mud? Earthquake nucleation and propagation through accretionary forearcs, *Geophys. Res. Lett.*, *38*(18), L18303, doi:10.1029/2011GL048552, 2011a.

Faulkner, D. R., T. M. Mitchell, E. Jensen, and J. Cembrano, Scaling of fault damage zones with displacement and the implications for fault growth processes, *J. Geophys. Res.*, *116*, B05403, doi:10.1029/2010JB007788, 2011b.

Fletcher, J. B., and A. McGarr, Moments, magnitudes, and radiated energies of non-volcanic tremor near Cholame, CA, from ground motion spectra at UPSAR, *Geophys. Res. Lett.*, *38*(16), L16314, doi:10.1029/2011GL048636, 2011.

Folesky, J., J. Kummerow, S. A. Shapiro, M. Häring, and H. Asanuma, Rupture directivity of fluid-induced microseismic events: Observations from an enhanced geothermal system, *J. Geophys. Res.*, *121*(11), 8034–8047, doi:10.1002/2016JB013078, 2016.

Fossum, A. F., and L. B. Freund, Nonuniformly moving shear crack model of a shallow focus earthquake mechanism, *J. Geophys. Res.*, *80*(23), 3347, doi:10.1029/JB080i023p03343, 1975.

Frank, W. B., N. M. Shapiro, V. Kostoglodov, A. L. Husker, M. Campillo, J. S. Payero, and G. A. Prieto, Low-frequency earthquakes in the Mexican Sweet Spot, *Geophys. Res. Lett.*, *40*(11), 2661–2666, doi:10.1002/grl.50561, 2013.

Frankel, A., High-frequency spectral falloff of earthquakes, fractal dimension of complex rupture, b value, and the scaling of strength on faults, *J. Geophys. Res.*, *96*, 6291–6302, doi:10.1029/91JB00237, 1991.

Fry, B., K. Chao, S. Bannister, Z. Peng, and L. Wallace, Deep tremor in New Zealand triggered by the 2010 Mw8.8 Chile earthquake, *Geophys. Res. Lett.*, *38*(15), L15306, doi:10.1029/2011GL048319, 2011.

Fusseis, F., M. R. Handy, and C. Schrank, Networking of shear zones at the brittle-to-viscous transition (Cap de Creus, NE Spain), *Journal of Structural Geology*, *28*(7), 1228–1243, doi:10.1016/j.jsg.2006.03.022, 2006.

Gao, H., D. A. Schmidt, and R. J. Weldon, Scaling relationships of source parameters for slow slip events, *Bull. Seis. Soc. Amer.*, *102*(1), 352–360, doi:10.1785/0120110096, 2012.

Ghosh, A., J. E. Vidale, and K. C. Creager, Tremor asperities in the transition zone control evolution of slow earthquakes, *J. Geophys. Res.*, *117*(B10), B10301, doi:10.1029/2012JB009249, 2012.

Gomberg, J., K. Creager, J. Sweet, J. Vidale, A. Ghosh, and A. Hotovec, Earthquake spectra and near-source attenuation in the Cascadia subduction zone, *J. Geophys. Res.*, *117*(B5), B05312, doi:10.1029/2011JB009055, 2012.

Got, J.-L., and J. Fréchet, Origins of amplitude variations in seismic doublets: Source or attenuation process?, *Geophys. J. Intern.*, *114*(2), 325–340, doi:10.1111/j.1365-246X.1993.tb03921.x, 1993.

Handy, M. R., G. Hirth, and R. Burgmann, Continental Fault Structure and Rheology from the Frictional-to-Viscous Transition Downwards, in *Tectonic Faults: Agents of Change on a Dynamic Earth (Dahlem Workshop 95, Berlin, January 2005)*, edited by M. R. Handy, G. Hirth, and N. Hovius, pp. 139–182, MIT Press, Cambridge, MA, 2007.

Hawthorne, J. C., and J.-P. Ampuero, A phase coherence approach to identifying co-located earthquakes and tremor, *Geophys. J. Intern.*, *209*(2), 623–642, doi:10.1093/gji/ggx012, 2017.

Hawthorne, J. C., and N. M. Bartlow, Observing and modeling the spectrum of a slow slip event, *J. Geophys. Res.*, *123*(5), 4243–4265, doi:10.1029/2017JB015124, 2018.

Hawthorne, J. C., and A. M. Rubin, Laterally propagating slow slip events in a rate and state friction model with a velocity-weakening to velocity-strengthening transition, *J. Geophys. Res.*, *118*(7), 3785–3808, doi:10.1002/jgrb.50261, 2013.

Hayman, N. W., and L. L. Lavier, The geologic record of deep episodic tremor and slip, *Geology*, *42*(3), 195–198, doi:10.1130/G34990.1, 2014.

Herrero, A., and P. Bernard, A kinematic self-similar rupture process for earthquakes, *Bull. Seis. Soc. Amer.*, *84*(4), 1216–1228, 1994.

Horowitz, F. G., and A. Ruina, Slip patterns in a spatially homogeneous fault model, *J. Geophys. Res.*, *94*(B8), 10,279–10,298, 1989.

Hough, S. E., Empirical Green's function analysis: Taking the next step, *J. Geophys. Res.*, *102*, 5369–5384, doi:10.1029/96JB03488, 1997.

Huang, Y., J.-P. Ampuero, and D. V. Helmberger, Earthquake ruptures modulated by waves in damaged fault zones, *J. Geophys. Res.*, *119*(4), 3133–3154, doi:10.1002/2013JB010724, 2014.

Ide, S., and S. Yabe, Universality of slow earthquakes in the very low frequency band, *Geophys. Res. Lett.*, *41*(8), 2786–2793, doi:10.1002/2014GL059712, 2014.

Ide, S., F. Imamura, Y. Yoshida, and K. Abe, Source characteristics of the Nicaraguan Tsunami Earthquake of September 2, 1992, *Geophys. Res. Lett.*, *20*(9), 863–866, doi:10.1029/93GL00683, 1993.

Ide, S., G. C. Beroza, D. R. Shelly, and T. Uchide, A scaling law for slow earthquakes, *Nature*, *447*(7140), 76–79, doi:10.1038/nature05780, 2007.

Ide, S., K. Imanishi, Y. Yoshida, G. C. Beroza, and D. R. Shelly, Bridging the gap between seismically and geodetically detected slow earthquakes, *Geophys. Res. Lett.*, *35*(10), L10305, doi:10.1029/2008GL034014, 2008.

Ihmlé, P. F., J.-M. Gomez, P. Heinrich, and S. Guibourg, The 1996 Peru tsunamigenic earthquake: Broadband source process, *Geophys. Res. Lett.*, *25*(14), 2691–2694, doi:10.1029/98GL01987, 1998.

Kanamori, H., and E. E. Brodsky, The physics of earthquakes, *Reports on Progress in Physics*, *67*(8), 1429–1496, doi:10.1088/0034-4885/67/8/R03, 2004.

Kanamori, H., and L. Rivera, Energy partitioning during an earthquake, *Washington DC American Geophysical Union Geophysical Monograph Series*, *170*, 3–13, doi:10.1029/170GM03, 2006.

Kane, D. L., P. M. Shearer, B. P. Goertz-Allmann, and F. L. Vernon, Rupture directivity of small earthquakes at Parkfield, *J. Geophys. Res.*, *118*(1), 212–221, doi:10.1029/2012JB009675, 2013.

Kano, M., A. Kato, R. Ando, and K. Obara, Strength of tremor patches along deep transition zone of a megathrust, *Scientific Reports*, *8*(1), 3655, doi:10.1038/s41598-018-22048-8, 2018.

Kato, A., Illuminating deep tremors along the Nankai subduction zone, Japan, by matched filter technique, *JpGU-AGU Joint Meeting*, pp. SSS04–02, 2017.

Kato, A., T. Iidaka, R. Ikuta, Y. Yoshida, K. Katsumata, T. Iwasaki, S. Sakai, C. Thurber, N. Tsumura, K. Yamaoka, T. Watanabe, T. Kunitomo, F. Yamazaki, M. Okubo, S. Suzuki, and N. Hirata, Variations of fluid pressure within the subducting oceanic crust and slow earthquakes, *Geophys. Res. Lett.*, *37*, L14310, doi:10.1029/2010GL043723, 2010.

Kennett, B. L. N., and E. R. Engdahl, Traveltimes for global earthquake location and phase identification, *Geophys. J. Intern.*, *105*(2), 429–465, doi:10.1111/j.1365-246X.1991.tb06724.x, 1991.

Kitajima, H., and D. M. Saffer, Elevated pore pressure and anomalously low stress in regions of low frequency earthquakes along the Nankai Trough subduction megathrust, *Geophys. Res. Lett.*, *39*(23), L23301, doi:10.1029/2012GL053793, 2012.

Kostrov, B. V., Unsteady propagation of longitudinal shear cracks, *Journal of Applied Mathematics and Mechanics*, *30*(6), 1241–1248, doi:10.1016/0021-8928(66)90087-6, 1966.

Kwiatek, G., K. Plenkers, G. Dresen, and J. R. Group, Source parameters of picoseismicity recorded at Mponeng deep gold mine, South Africa: implications for scaling relations, *Bull. Seis. Soc. Amer.*, *101*(6), 2592–2608, doi:10.1785/0120110094, 2011.

Langer, J. S., J. M. Carlson, C. R. Myers, and B. E. Shaw, Slip complexity in dynamic models of earthquake faults, *Proceedings of the National Academy of Sciences*, *93*(9), 3825–3829, doi:10.1073/pnas.93.9.3825, 1996.

Leclère, H., F. Cappa, D. Faulkner, O. Fabbri, P. Armitage, and O. Blake, Development and maintenance of fluid overpressures in crustal fault zones by elastic compaction and implications for earthquake swarms, *J. Geophys. Res.*, *120*(6), 4450–4473, doi:10.1002/2014JB011759, 2015.

Lengliné, O., and J.-L. Got, Rupture directivity of microearthquake sequences near Parkfield, California, *Geophys. Res. Lett.*, *38*, L08310, doi:10.1029/2011GL047303, 2011.

Lengliné, O., W. B. Frank, D. Marsan, and J. P. Ampuero, Imbricated slip rate processes during slow slip transients imaged by low-frequency earthquakes, *Earth Planet. Sci. Lett.*, *476*, 122–131, doi:10.1016/j.epsl.2017.07.032, 2017.

Lewis, M. A., and Y. Ben-Zion, Diversity of fault zone damage and trapping structures in the Parkfield section of the San Andreas Fault from comprehensive analysis of near fault seismograms, *Geophys. J. Intern.*, *183*(3), 1579–1595, doi:10.1111/j.1365-246X.2010.04816.x, 2010.

Li, Y.-G., R. D. Catchings, and M. R. Goldman, Subsurface fault damage zone of the 2014 Mw 6.0 South Napa, California, earthquake viewed from fault-zone trapped waves, *Bull. Seis. Soc. Amer.*, *106*(6), 2747–2763, doi:10.1785/0120160039, 2016.

Lin, G., C. H. Thurber, H. Zhang, E. Hauksson, P. M. Shearer, F. Waldhauser, T. M. Brocher, and J. Hardebeck, A California statewide three-dimensional seismic velocity model from both absolute and differential times, *Bull. Seis. Soc. Amer.*, *100*(1), 225–240, doi:10.1785/0120090028, 2010.

Liu, L., M. Gurnis, M. Seton, J. Saleeby, R. D. Muller, and J. M. Jackson, The role of oceanic plateau subduction in the Laramide orogeny, *Nat. Geosci.*, *3*(5), 353–357, doi:10.1038/ngeo829, 2010.

Liu, Y. J., and J. R. Rice, Aseismic slip transients emerge spontaneously in three-dimensional rate and state modeling of subduction earthquake sequences, *J. Geophys. Res.*, *110*, B08307, doi:10.1029/2004JB003424, 2005.

Liu, Y. J., and J. R. Rice, Spontaneous and triggered aseismic deformation transients in a subduction fault model, *J. Geophys. Res.*, *112*(B9), B09404, doi:10.1029/2007JB004930, 2007.

Luo, Y., and J.-P. Ampuero, Tremor migration patterns and the collective behavior of deep asperities mediated by creep, *EarthArXiv*, doi:10.17605/OSF.IO/MBCAV, 2017.

Ma, S., A self-consistent mechanism for slow dynamic deformation and large tsunami generation for earthquakes in the shallow subduction zone, *Geophys. Res. Lett.*, *39*(11), L11310, doi:10.1029/2012GL051854, 2012.

Madariaga, R., Seismic source theory, in *Treatise on Geophysics*, vol. 4: Earthquake Seismology, edited by H. Kanamori and G. Schubert, p. 6054, Elsevier, Amsterdam, 2007.

Maeda, T., and K. Obara, Spatiotemporal distribution of seismic energy radiation from low-frequency tremor in western Shikoku, Japan, *J. Geophys. Res.*, *114*, B00A09, doi:10.1029/2008JB006043, 2009.

Mai, P. M., and G. C. Beroza, A spatial random field model to characterize complexity in earthquake slip, *J. Geophys. Res.*, *107*(B11), 2308, doi:10.1029/2001JB000588, 2002.

McGuire, J. J., Estimating finite source properties of small earthquake ruptures, *Bull. Seis. Soc. Amer.*, *94*(2), 377–393, doi:10.1785/0120030091, 2004.

Melgar, D., and G. P. Hayes, Systematic observations of the slip pulse properties of large earthquake ruptures, *Geophys. Res. Lett.*, *44*(19), 9691–9698, doi:10.1002/2017GL074916, 2017.

Mori, J., and A. Frankel, Source parameters for small events associated with the 1986 North Palm Springs, California, earthquake determined using empirical Green functions, *Bull. Seis. Soc. Amer.*, *80*(2), 278–295, 1990.

Mueller, C. S., Source pulse enhancement by deconvolution of an empirical Green's function, *Geophys. Res. Lett.*, *12*(1), 33–36, doi:10.1029/GL012i001p00033, 1985.

Nakata, R., R. Ando, T. Hori, and S. Ide, Generation mechanism of slow earthquakes: Numerical analysis based on a dynamic model with brittle-ductile mixed fault heterogeneity, *J. Geophys. Res.*, *116*(B8), B08308, doi:10.1029/2010JB008188, 2011.

Nowack, R. L., and M. G. Bostock, Scattered waves from low-frequency earthquakes and plate boundary structure in northern Cascadia, *Geophys. Res. Lett.*, *40*(16), 4238–4243, doi:10.1002/grl.50826, 2013.

Obara, K., Nonvolcanic deep tremor associated with subduction in southwest Japan, *Science*, *296*(5573), 1679–1681, doi:10.1126/science.1070378, 2002.

Payero, J. S., V. Kostoglodov, N. Shapiro, T. Mikumo, A. Iglesias, X. Perez-Campos, and R. W. Clayton, Nonvolcanic tremor observed in the Mexican subduction zone, *Geophys. Res. Lett.*, *35*, L07305, doi:10.1029/2007GL032877, 2008.

Perfettini, H., and J. P. Ampuero, Dynamics of a velocity strengthening fault region: Implications for slow earthquakes and postseismic slip, *J. Geophys. Res.*, *113*, B09411, doi:10.1029/2007JB005398, 2008.

Peterson, C. L., and D. H. Christensen, Possible relationship between nonvolcanic tremor and the 1998–2001 slow slip event, south central Alaska, *J. Geophys. Res.*, *114*, B06302, doi:10.1029/2008JB006096, 2009.

Polet, J., and H. Kanamori, Tsunami earthquakes, in *Encyclopedia of complexity and systems science*, pp. 9577–9592, Springer, New York, 2009.

Poulet, T., E. Veveakis, K. Regenauer-Lieb, and D. A. Yuen, Thermo-poro-mechanics of chemically active creeping faults: 3. The role of serpentinite in episodic tremor and slip sequences, and transition to chaos, *J. Geophys. Res.*, *119*(6), 4606–4625, doi:10.1002/2014JB011004, 00001, 2014.

Prieto, G. A., P. M. Shearer, F. L. Vernon, and D. Kilb, Earthquake source scaling and self-similarity estimation from stacking P and S spectra, *J. Geophys. Res.*, *109*(B8), B08310, doi:10.1029/2004JB003084, 2004.

Rempe, M., T. Mitchell, J. Renner, S. Nippress, Y. Ben-Zion, and T. Rockwell, Damage and seismic velocity structure of pulverized rocks near the San Andreas Fault, *J. Geophys. Res.*, *118*(6), 2813–2831, doi:10.1002/jgrb.50184, 2013.

Rice, J. R., The mechanics of earthquake rupture, in *Physics of the Earth's Interior (Proc. Intl. School of Physics "E. Fermi" Course 78)*, edited by A. M. Dziewonski and E. Boschi, pp. 555–650, Italian Physical Society / North Holland Publishing Co., 1980.

Rogers, G., and H. Dragert, Episodic tremor and slip on the Cascadia subduction zone: the chatter of silent slip, *Science*, *300*(5627), 1942–1943, doi:10.1126/science.1084783, 2003.

Roten, D., K. B. Olsen, and S. M. Day, Off-fault deformations and shallow slip deficit from dynamic rupture simulations with fault zone plasticity, *Geophys. Res. Lett.*, *44*(15), 7733–7742, doi:10.1002/2017GL074323, 2017.

Rowe, C. D., F. Meneghini, and J. C. Moore, Fluid-rich damage zone of an ancient out-of-sequence thrust, Kodiak Islands, Alaska, *Tectonics*, *28*, 1–20, doi:10.1029/2007TC002126, 2009.

Royer, A. A., and M. G. Bostock, A comparative study of low frequency earthquake templates in northern Cascadia, *Earth Planet. Sci. Lett.*, *402*, 247–256, doi:10.1016/j.epsl.2013.08.040, 2014.

Royer, A. A., A. M. Thomas, and M. G. Bostock, Tidal modulation and triggering of low-frequency earthquakes in northern Cascadia, *J. Geophys. Res.*, *120*(1), 384–405, doi: 10.1002/2014JB011430, 2015.

Rubin, A. M., Episodic slow slip events and rate-and-state friction, *J. Geophys. Res.*, *113*, B11414, doi:10.1029/2008JB005642, 2008.

Rubin, A. M., Properties of Creep Fronts on Rate-and-State Faults, *Eos Trans. AGU, Fall Meeting Suppl.*, *21*, T21F–08, 2009.

Rubin, A. M., and J. G. Armbruster, Imaging slow slip fronts in Cascadia with high precision cross-station tremor locations, *Geochem., Geophys., Geosyst.*, pp. 5371–5392, doi: 10.1002/2013GC005031, 2013.

Rubin, A. M., and M. G. Bostock, What is This Thing Called Tremor?, *Eos Trans. AGU, Fall Meeting Suppl.*, *52*, 2017.

Rubinstein, J. L., D. R. Shelly, and W. L. Ellsworth, Non-volcanic tremor: a window into the roots of fault zones, in *New Frontiers in Integrated Solid Earth Sciences*, edited by J. Negendank and S. Cloetingh, pp. 287–314, Springer, Dordrecht, 2009.

Saffer, D. M., and L. M. Wallace, The frictional, hydrologic, metamorphic and thermal habitat of shallow slow earthquakes, *Nat. Geosci.*, *8*(8), 594–600, doi:10.1038/ngeo2490, 2015.

Savard, G., and M. G. Bostock, Detection and location of low-frequency earthquakes using cross-station correlation, *Bull. Seis. Soc. Amer.*, *105*(4), 2128–2142, doi:10.1785/0120140301, 2015.

Seekins, L. C., and J. Boatwright, Rupture directivity of moderate earthquakes in northern California, *Bull. Seis. Soc. Amer.*, *100*(3), 1107–1119, doi:10.1785/0120090161, 2010.

Segall, P., A. M. Rubin, A. M. Bradley, and J. R. Rice, Dilatant strengthening as a mechanism for slow slip events, *J. Geophys. Res.*, *115*, B12305, doi:10.1029/2010JB007449, 2010.

Seno, T., and T. Yamasaki, Low-frequency tremors, intraslab and interplate earthquakes in Southwest Japan-from a viewpoint of slab dehydration, *Geophys. Res. Lett.*, *30*(22), 1–4, doi: 10.1029/2003GL018349, 2003.

Shaw, B. E., and J. R. Rice, Existence of continuum complexity in the elastodynamics of repeated fault ruptures, *J. Geophys. Res.*, *105*(B10), 23,791–23,810, doi:10.1029/2000JB900203, 2000.

Shearer, P., *Introduction to Seismology*, 2 ed., Cambridge University Press, Cambridge, UK, 2009.

Shelly, D. R., Migrating tremors illuminate complex deformation beneath the seismogenic San Andreas fault, *Nature*, *463*(7281), 648–652, doi:10.1038/nature08755, 2010a.

Shelly, D. R., Periodic, chaotic, and doubled earthquake recurrence intervals on the deep San Andreas Fault, *Science*, *328*(5984), 1385–1388, doi:10.1126/science.1189741, 2010b.

Shelly, D. R., A 15 year catalog of more than 1 million low-frequency earthquakes: Tracking tremor and slip along the deep San Andreas Fault, *J. Geophys. Res.*, *122*(5), 3739–3753, doi: 10.1002/2017JB014047, 2017.

Shelly, D. R., and J. L. Hardebeck, Precise tremor source locations and amplitude variations along the lower-crustal central San Andreas Fault, *Geophys. Res. Lett.*, *37*, L14301, doi: 10.1029/2010GL043672, 2010.

Shelly, D. R., G. C. Beroza, S. Ide, and S. Nakamula, Low-frequency earthquakes in Shikoku, Japan, and their relationship to episodic tremor and slip, *Nature*, *442*(7099), 188–191, doi: 10.1038/nature04931, 2006.

Shelly, D. R., G. C. Beroza, and S. Ide, Non-volcanic tremor and low-frequency earthquake swarms, *Nature*, *446*(7133), 305–307, doi:10.1038/nature05666, 2007.

Shelly, D. R., W. L. Ellsworth, T. Ryberg, C. Haberland, G. S. Fuis, J. Murphy, R. M. Nadeau, and R. Bürgmann, Precise location of San Andreas Fault tremors near Cholame, California using seismometer clusters: Slip on the deep extension of the fault?, *Geophys. Res. Lett.*, *36*(1), L01303, doi:10.1029/2008GL036367, 2009.

Shibazaki, B., and Y. Iio, On the physical mechanism of silent slip events along the deeper part of the seismogenic zone, *Geophys. Res. Lett.*, *30*(9), 1–4, doi:10.1029/2003GL017047, 2003.

Shibazaki, B., and T. Shimamoto, Modelling of short-interval silent slip events in deeper subduction interfaces considering the frictional properties at the unstable-stable transition regime, *Geophys. J. Intern.*, *171*(1), 191–205, doi:10.1111/j.1365-246X.2007.03434.x, 2007.

Shipton, Z. K., and P. A. Cowie, Damage zone and slip-surface evolution over μm to km scales in high-porosity Navajo sandstone, Utah, *Journal of Structural Geology*, *23*(12), 1825–1844, doi:10.1016/S0191-8141(01)00035-9, 2001.

Skarbek, R. M., A. W. Rempel, and D. A. Schmidt, Geologic heterogeneity can produce aseismic slip transients, *Geophys. Res. Lett.*, *39*(21), L21306, doi:10.1029/2012GL053762, 2012.

Song, T.-R. A., D. V. Helmberger, M. R. Brudzinski, R. W. Clayton, P. Davis, X. Perez-Campos, and S. K. Singh, Subducting slab ultra-slow velocity layer coincident with silent earthquakes in southern Mexico, *Science*, *324*(5926), 502–506, doi:10.1126/science.1167595, 2009.

Stefano, R. D., C. Chiarabba, L. Chiaraluce, M. Cocco, P. D. Gori, D. Piccinini, and L. Valoroso, Fault zone properties affecting the rupture evolution of the 2009 (Mw 6.1) L'Aquila earthquake (central Italy): Insights from seismic tomography, *Geophys. Res. Lett.*, *38*, L10310, doi:10.1029/2011GL047365, 2011.

Sweet, J. R., K. C. Creager, and H. Houston, A family of repeating low-frequency earthquakes at the downdip edge of tremor and slip, *Geochem., Geophys., Geosyst.*, *15*(9), 3713–3721, doi: 10.1002/2014GC005449, 2014.

Taira, T., D. S. Dreger, and R. M. Nadeau, Rupture process for micro-earthquakes inferred from borehole seismic recordings, *International Journal of Earth Sciences*, *104*(6), 1499–1510, doi: 10.1007/s00531-015-1217-8, 2015.

Thomas, A. M., G. C. Beroza, and D. R. Shelly, Constraints on the source parameters of low-frequency earthquakes on the San Andreas Fault, *Geophys. Res. Lett.*, *43*(4), 1464–1471, doi: 10.1002/2015GL067173, 2016.

Thomas, A. M., N. M. Beeler, Q. Bletery, R. Burgmann, and D. R. Shelly, Using low-frequency earthquake families on the San Andreas Fault as deep creepmeters, *J. Geophys. Res.*, *123*(1), 457–475, doi:10.1002/2017JB014404, 2018.

Thomson, D. J., Spectrum estimation and harmonic analysis, *Proc. IEEE*, *70*(9), 1055–1096, doi: 10.1109/PROC.1982.12433, 1982.

Tinti, E., E. Fukuyama, A. Piatanesi, and M. Cocco, A kinematic source-time function compatible with earthquake dynamics, *Bull. Seis. Soc. Amer.*, *95*(4), 1211–1223, doi:10.1785/0120040177, 2005.

Uchide, T., P. M. Shearer, and K. Imanishi, Stress drop variations among small earthquakes before the 2011 Tohoku-oki, Japan, earthquake and implications for the main shock, *J. Geophys. Res.*, *119*(9), 7164–7174, doi:10.1002/2014JB010943, 2014.

Ujiie, K., H. Saishu, Å. Fagereng, N. Nishiyama, M. Otsubo, H. Masuyama, and H. Kagi, An explanation of episodic tremor and slow slip constrained by crack-seal veins and viscous shear in subduction mélange, *Geophys. Res. Lett.*, *45*, 5371–5379, doi:10.1029/2018GL078374, 2018.

van Avendonk, H. J. A., W. S. Holbrook, D. Lizarralde, M. M. Mora, S. Harder, A. D. Bullock, G. E. Alvarado, and C. J. Ramírez, Seismic evidence for fluids in fault zones on top of the subducting Cocos Plate beneath Costa Rica, *Geophys. J. Intern.*, *181*(2), 997–1016, doi: 10.1111/j.1365-246X.2010.04552.x, 2010.

Veedu, D. M., and S. Barbot, The Parkfield tremors reveal slow and fast ruptures on the same asperity, *Nature*, *532*, 361–365, doi:10.1038/nature17190, 2016.

Velasco, A. A., C. J. Ammon, and T. Lay, Empirical green function deconvolution of broadband surface waves: Rupture directivity of the 1992 Landers, California (Mw = 7.3), earthquake, *Bull. Seis. Soc. Amer.*, *84*(3), 735–750, 1994.

Venkataraman, A., and H. Kanamori, Observational constraints on the fracture energy of subduction zone earthquakes, *J. Geophys. Res.*, *109*(B5), B05302, doi:10.1029/2003JB002549, 2004.

Veveakis, E., T. Poulet, and S. Alevizos, Thermo-poro-mechanics of chemically active creeping faults: 2. Transient considerations, *J. Geophys. Res.*, *119*(6), 4583–4605, doi: 10.1002/2013JB010071, 2014.

Waldhauser, F., Near-real-time double-difference event location using long-term seismic archives, with application to northern California, *Bull. Seis. Soc. Amer.*, *99*(5), 2736–2748, doi: 10.1785/0120080294, 2009.

Walter, J. I., S. Y. Schwartz, J. M. Protti, and V. Gonzalez, Persistent tremor within the northern Costa Rica seismogenic zone, *Geophys. Res. Lett.*, *38*, L01307, doi:10.1029/2010GL045586, 2011.

Wang, E., and A. M. Rubin, Rupture directivity of microearthquakes on the San Andreas Fault from spectral ratio inversion, *Geophys. J. Intern.*, *186*(2), 852–866, doi:10.1111/j.1365-246X.2011.05087.x, 2011.

Watanabe, T., Y. Hiramatsu, and K. Obara, Scaling relationship between the duration and the amplitude of non-volcanic deep low-frequency tremors, *Geophys. Res. Lett.*, *34*(7), L07305, doi:10.1029/2007GL029391, 2007.

Webber, S., S. Ellis, and Å. Fagereng, "Virtual shear box" experiments of stress and slip cycling within a subduction interface mélange, *Earth Planet. Sci. Lett.*, *488*, 27–35, doi:10.1016/j.epsl.2018.01.035, 2018.

Wech, A. G., and K. C. Creager, Cascadia tremor polarization evidence for plate interface slip, *Geophys. Res. Lett.*, *34*(22), doi:10.1029/2007GL031167, 2007.

Yabe, S., and S. Ide, Spatial distribution of seismic energy rate of tectonic tremors in subduction zones, *J. Geophys. Res.*, *119*(11), 8171–8185, doi:10.1002/2014JB011383, 2014.

Yabe, S., and S. Ide, Slip-behavior transitions of a heterogeneous linear fault, *J. Geophys. Res.*, *122*(1), 387–410, doi:10.1002/2016JB013132, 2017.

Yabe, S., A. S. Baltay, S. Ide, and G. C. Beroza, Seismic-wave attenuation determined from tectonic tremor in multiple subduction zonesseismic-wave attenuation determined from tectonic tremor in multiple subduction zones, *Bull. Seis. Soc. Amer.*, *104*(4), 2043–2059, doi:10.1785/0120140032, 2014.

Yang, H., Z. Li, Z. Peng, Y. Ben-Zion, and F. Vernon, Low-velocity zones along the San Jacinto Fault, Southern California, from body waves recorded in dense linear arrays, *J. Geophys. Res.*, *119*(12), 8976–8990, doi:10.1002/2014JB011548, 2014.

Ye, L., T. Lay, H. Kanamori, and L. Rivera, Rupture characteristics of major and great (Mw ¿= 7.0) megathrust earthquakes from 1990 to 2015: 1. Source parameter scaling relationships, *J. Geophys. Res.*, *121*(2), 826–844, doi:10.1002/2015JB012426, 2016.

Zhang, J., P. Gerstoft, P. M. Shearer, H. Yao, J. E. Vidale, H. Houston, and A. Ghosh, Cascadia tremor spectra: Low corner frequencies and earthquake-like high-frequency falloff, *Geochem., Geophys., Geosyst.*, *12*(10), Q10007, doi:10.1029/2011GC003759, 2011.